Structure and phases of the Au(111) surface: X-ray-scattering measurements

A. R. Sandy and S. G. J. Mochrie
Department of Physics, Massachusetts Institute of Technology, Cambridge, Massachusetts 02139-4307

D. M. Zehner
Solid State Division, Oak Ridge National Laboratory, Oak Ridge, Tennessee 37831-6057

K. G. Huang and Doon Gibbs
Department of Physics, Brookhaven National Laboratory, Upton, New York 11973-5000
(Received 10 September 1990)

The results of a comprehensive synchrotron x-ray-scattering study of the clean, reconstructed Au(111) surface between 300 and 1250 K are presented. Two surface phases are identified and characterized. For $T < 865$ K, the reconstruction consists of a series of discommensurations, separating surface regions with the correct face-centered-cubic (fcc) *ABC* stacking sequence from regions with a faulted *ABA* stacking sequence. A key feature of this phase is the existence of an equilibrium density of kinks between rotationally equivalent domains. At 865 K, the reconstruction starts to lose long-range order. The first-order transformation to a disordered phase is complete by 880 K. In this phase, the topmost layer has hexagonal symmetry and is on the average isotropically compressed compared with bulk (111) planes. Between 880 and 1250 K the translational correlation length and the average compression of the overlayer evolve only slightly. Interpretation of the x-ray reflectivity, both specular and nonspecular, establishes, however, that the occupation of fcc *C* sites and faulted *A* sites is approximately constant throughout the temperature range studied. In addition, the separation between the top two layers is expanded 3% relative to the bulk (111) interlayer spacing and the surface-normal vibrational amplitude in the surface layers is enhanced with respect to the bulk value.

I. INTRODUCTION

Perhaps the most surprising reconstruction of a metal surface is that of the close-packed (111) face of gold. The ideal (111) surface of an elemental face-centered-cubic (fcc) material is hexagonally close packed. This appears to be the lowest-energy configuration of the (111) surface of most fcc metals. In contrast, the Au(111) surface layer is denser than the bulk (111) planes. This reconstruction has been studied by a variety of experimental techniques.[1-10] As a result, it is believed that at room temperature the reconstruction is comprised of a series of linear discommensurations running parallel to the $\langle 11\bar{2} \rangle$ directions separating surface regions with the correct face-centered-cubic *ABC* stacking sequence from regions with a faulted *ABA* stacking sequence $[(s \times \sqrt{3})$ reconstruction, with $s \equiv 23]$. Such a phase, incommensurate in only one direction, is often called a *stripe-domain* phase.[11] Little is known, however, about the structural behavior of the Au(111) surface at elevated temperatures. For this reason, we have carried out a comprehensive synchrotron x-ray diffraction study of the clean Au(111) surface between 300 and 1250 K. Our results have particular relevance to the suggestion that the relief of surface stress gives rise to the Au(111) reconstruction[12-14] and to recent predictions that high-symmetry surfaces, which reconstruct into one of several rotationally equivalent structures, are unstable to the formation of domains.[15] A complete account of our procedures, data, and analysis is given in this paper; a summary has appeared previously.[16]

We have identified and characterized two distinct phases. For sample temperatures less than 865 K, the surface structure is well ordered. However, the x-ray diffraction pattern cannot be understood on the basis of the stripe-domain reconstruction described above. Instead, its interpretation leads to a structural model involving an *equilibrium* density of kinks separating domains whose discommensuration orientations differ by 120°. The kinks are themselves ordered and produce a structure in which two of the three possible rotationally equivalent domains of the stripe-domain structure alternate periodically across the surface. We call this the chevron phase. The presence of isolated kinks is evident in the transmission electron microscopy (TEM) studies of Refs. 4 and 5, and in the scanning tunneling microscopy (STM) study of Ref. 10. Very recently, we have learned of elegant STM results that independently lead to the same structural model at 300 K.[17] The appearance of differently oriented domains suggests that there are competing interactions which compromise at the equilibrium kink separation. Vanderbilt[18] has suggested that a possible origin of this phenomenon may lie in the anisotropic stress that arises when a surface reconstructs with a broken orientational symmetry.[15]

The chevron structure is characterized by two incommensurate wave vectors: the discommensuration wave vector δ_D and the kink wave vector δ_K. Both wave vectors increase monotonically with increasing temperature,

which corresponds to an overall contraction of the chevron unit cell relative to the bulk lattice constants. The average discommensuration periodicity varies smoothly from $L_D = 22.5a$ at 300 K to $L_D = 20.9a$ at 850 K, where a is the ideal fcc nearest-neighbor separation. (At 300 K, $a = 2.885$ Å.) The average kink periodicity is approximately constant between 300 and 700 K ($L_K = 112.4a \cong 324.3$ Å) and decreases rapidly between 700 and 850 K (at which temperature $L_K = 70.4a = 204.9$ Å). The ratio of the two wave vectors (δ_K/δ_D) varies from $\cong 0.2$ at 300 K to $\cong 0.3$ at 850 K. Remarkably, the kink ordering extends the farthest when the ratio is close to one-quarter. At one-quarter, the unit-cell dimensions are such that the distance between kinks, perpendicular to the discommensurations, exactly equals four complete discommensuration periods. With regard to the chevron model, it is important to add that calculated intensities based on the chevron structure quantitatively describe the observed variation of the peak intensities with the ratio δ_K/δ_D.

At 865 K, the reconstruction begins to lose long-range order. The transformation to a partially disordered phase is complete by 880 K. However, there is no accompanying surface roughening[19–21] or surface melting.[22] Results of x-ray reflectivity measurements, both specular and nonspecular,[23–26] establish that for length scales less than the translational correlation length (ξ) the surface is well ordered with the atoms in the topmost layer occupying well-defined atomic positions up to the highest temperatures studied.[27] In this phase, the topmost layer exhibits hexagonal symmetry and is on the average isotropically, but not uniformly, compressed relative to the bulk Au(111) planes. Remarkably, the translational correlation length is only weakly temperature dependent ($\xi \cong 105$ Å) between 900 and 1250 K. Furthermore, it barely exceeds the surface periodicity (70 Å). In this respect, the configuration of faulted and unfaulted regions is very disordered. For this reason we call this phase the discommensuration fluid phase.[28–30] Near the phase transformation, there is an evolution of the discommensuration-fluid-phase scattering function; however, the transformation to the chevron phase is discontinuous (first order).

The only previous study that included measurements performed at high temperatures was the TEM study of Ref. 5, where the low-temperature phase was observed to evolve gradually to a disordered phase over a wide range of temperature. In contrast, we observe a narrow temperature range of coexistence between the two phases (15 K). In the TEM study, the reconstruction was observed to disappear by 1170 K. However, we find that the surface is still reconstructed at 1250 K.[27]

Further results of the present study, which emerge from an analysis of the x-ray reflectivity, include a determination that the layer spacing between the topmost and second layer (d_{01}) is expanded by 3% relative to the bulk (111) interlayer spacing. In addition, we find a nearly sinusoidal variation of the displacement field from faulted to unfaulted regions and that the ratio of sizes of the faulted and unfaulted regions is 0.7. Finally, we emphasize that only the topmost layer participates in the reconstruction, in contrast to the suggestion of Ref. 7 that there are two layers with lattice constants different from those of the bulk.

The format of this paper is as follows: We review the relevant features of x-ray scattering as applied to surface structures and describe our experimental procedures in Sec. II. In Sec. III we present our data. Section III A describes measurements of the x-ray reflectivity of the Au(111) surface, both specular and nonspecular, for temperatures between 300 and 1250 K. Fine-resolution, glancing incidence measurements of the in-plane diffraction pattern for the chevron phase are reported in Sec. III B. Section III C details fine-resolution measurements of the discommensuration-fluid-phase scattering function, while Sec. III D describes details of the phase transformation. Finally, in Sec. IV, we present our conclusions.

II. METHODS AND PROCEDURES

A. Scattering geometry and coordinate system

As shown in Sec. II B, the x-ray-scattering cross section from a crystal surface consists of lines in reciprocal space, which extend from Bragg reflections of the bulk crystal in directions normal to the surface (truncation rods). If the surface exhibits a reconstruction, there are, in addition, lines of scattering through the new wave vectors which are associated with the reconstruction (overlayer rods). The overlayer rods are also normal to the surface. Figure 1 shows a schematic view of the reciprocal space of a (111) terminated Au crystal. (For clarity we do not show the overlayer rods.) Because of its threefold rotational symmetry about the surface normal—the cubic [111] direction—the points at which the truncation rods (heavy lines) intersect the surface plane are arranged on a hexagonal lattice. It is therefore convenient to employ a hexagonal coordinate system, which is related to

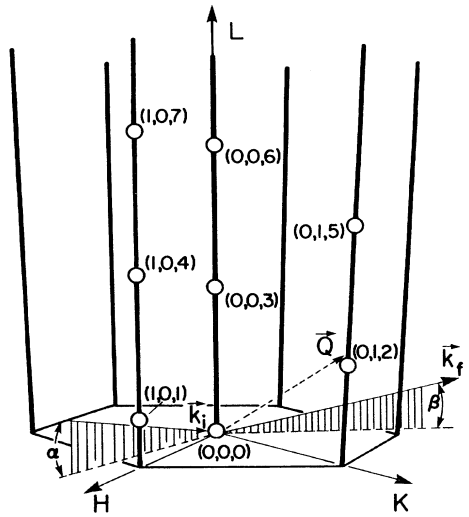

FIG. 1. Reciprocal space as defined by the hexagonal coordinate system. The scattering geometry and positions of bulk Bragg reflections (open circles) are also illustrated.

the cubic coordinate system as follows.[31] For the cubic system, we define $\mathbf{a}_1$, $\mathbf{a}_2$, and $\mathbf{a}_3$ to be vectors that span the conventional fcc unit cell, with $|\mathbf{a}_1|=|\mathbf{a}_2|=|\mathbf{a}_3|=a_0$, where a_0 is the length of the side of the unit cell. (At 300 K, $a_0=4.078$ Å.) We take them to lie along the x, y, and z directions, respectively. We also define $a\equiv a_0/\sqrt{2}$, which is the ideal nearest-neighbor separation. The real-space hexagonal coordinate system is then given by

$$\mathbf{A}_1=-\mathbf{a}_1/2+\mathbf{a}_2/2=a_0(-\tfrac{1}{2},\tfrac{1}{2},0)_{\text{cubic}} ,$$

$$\mathbf{A}_2=-\mathbf{a}_2/2+\mathbf{a}_3/2=a_0(0,-\tfrac{1}{2},\tfrac{1}{2})_{\text{cubic}} ,$$

and

$$\mathbf{A}_3=\mathbf{a}_1+\mathbf{a}_2+\mathbf{a}_3=a_0(1,1,1)_{\text{cubic}} .$$

$\mathbf{A}_1$ and $\mathbf{A}_2$ point to nearest-neighbor atoms 120° apart on an ideal fcc (111) plane and $\mathbf{A}_3$ is normal to that plane. When viewed along the surface-normal direction, an ideal fcc crystal is composed of hexagonally close-packed layers separated along the surface-normal direction by $|\mathbf{A}_3|/3$. In addition, the layers are translated from each other in the periodic sequence $ABCABC\ldots$ with in-plane translations $\boldsymbol{\delta}_A=-\boldsymbol{\delta}_C=(\mathbf{A}_1-\mathbf{A}_2)/3$ and $\boldsymbol{\delta}_B=0$. The reciprocal basis of the hexagonal coordinate system is given by

$$\mathbf{B}_1=2\pi/a_0(-\tfrac{4}{3},\tfrac{2}{3},\tfrac{2}{3})_{\text{cubic}} ,$$

$$\mathbf{B}_2=2\pi/a_0(-\tfrac{2}{3},-\tfrac{2}{3},\tfrac{4}{3})_{\text{cubic}} ,$$

and

$$\mathbf{B}_3=2\pi/a_0(\tfrac{1}{3},\tfrac{1}{3},\tfrac{1}{3})_{\text{cubic}} .$$

An arbitrary vector in reciprocal space, $\mathbf{G}$, is referenced in the hexagonal reciprocal basis by the indices H, K, and L and in the cubic reciprocal basis by the indices h, k, and l. Thus,

$$\mathbf{G}=H\mathbf{B}_1+K\mathbf{B}_2+L\mathbf{B}_3=h\mathbf{b}_1+k\mathbf{b}_2+l\mathbf{b}_3 ,$$

where $\mathbf{b}_1$, $\mathbf{b}_2$, and $\mathbf{b}_3$ are reciprocal-lattice vectors of the cubic coordinate system. In the hexagonal coordinate system, the wave-vector transfer normal to the surface is labeled by the single index L. This coordinate system is employed in Fig. 1. The units of the reciprocal coordinate system are as follows: for wave-vector transfers parallel to the surface the units are $a^*=4\pi/\sqrt{3}a=2.52$ Å^{-1} at 300 K and for positions along the surface-normal direction, $c^*=2\pi/\sqrt{3}a_0=0.89$ Å^{-1} at 300 K. The above relation for $\mathbf{G}$ allows us to solve for the cubic indices hkl in terms of the indices HKL of the hexagonal coordinate system and vice versa. The solutions for the cubic indices in terms of the hexagonal indices are $h=-4H/3-2K/3+L/3$, $k=2H/3-2K/3+L/3$, and $l=2H/3+4K/3+L/3$. For example, $(1,1,1)_{\text{cubic}}=(0,0,3)$, $(\bar{1},1,1)_{\text{cubic}}=(1,0,1)$, $(0,2,2)_{\text{cubic}}=(1,0,4)$, $(0,0,2)_{\text{cubic}}=(0,1,2)$, and $(1,1,3)_{\text{cubic}}=(0,1,5)$. Henceforth, we will always denote positions in reciprocal space and real space by means of the hexagonal coordinates. In Fig. 1 the wave vector of the incident ($\mathbf{k}_i$) and scattered ($\mathbf{k}_f$) x rays are shown subtending angles α and β, respectively, with the surface plane. The scattering wave vector is $\mathbf{Q}=\mathbf{k}_f-\mathbf{k}_i$. By suitably varying the scattering angle (2θ) and the crystal orientation, it is possible to measure the scattered x-ray intensity along each rod of scattering. We refer to that scattered intensity, normalized by the incident intensity, as the x-ray reflectivity.

B. X-ray cross section

In this subsection we write down a general expression for the x-ray-scattering cross section and then apply it to the scattering from surface structures. For monochromatic x rays incident on a sample, let $g(\theta_1,\psi_1)d\theta_1 d\psi_1$ be the probability that an x ray is incident between θ_1 and $\theta_1+d\theta_1$ within the scattering plane (in plane) and between ψ_1 and $\psi_1+d\psi_1$ perpendicular to the scattering plane (out of plane).[32] If all incident x rays strike the sample, we have

$$\int g(\theta_1,\psi_1)d\theta_1 d\psi_1=1 . \tag{1}$$

After the sample, x rays are scattered at an angle θ_2 within the diffraction plane and ψ_2 out of the diffraction plane. If the detector acceptance is described by a function $G(\theta_2,\psi_2)$, the number of photons per second scattered into the detector (n_s) divided by the number incident (n_i) is

$$n_s/n_i=\frac{1}{A_0}\int d\theta_1 d\theta_2 d\psi_1 d\psi_2 g(\theta_1,\psi_1)G(\theta_2,\psi_2)d\sigma/d\Omega , \tag{2}$$

where $d\sigma/d\Omega$ is the x-ray-scattering cross section, n_i is the number of x rays incident per second, and A_0 is the cross-sectional area of the incident beam. For diffuse scattering, $d\sigma/d\Omega$ depends smoothly on angle and may be brought outside of the integral:

$$\begin{aligned} n_s/n_i&=\frac{1}{A_0}(d\sigma/d\Omega)\Delta\theta_2\Delta\psi_2 \\ &=\frac{1}{A_0}(d\sigma/d\Omega)\Delta\Omega=\frac{1}{A_0}r_0^2 S(\mathbf{Q})\Delta\Omega , \end{aligned} \tag{3}$$

where $\Delta\Omega$ is the total (solid angular) acceptance of the detector and $r_0=2.818\times10^{-15}$ m is the Thomson radius. This equation defines the scattering function $S(\mathbf{Q})$, which is a function of only the wave-vector transfer ($\mathbf{Q}$).

The x-ray-scattering cross section from a crystal with a well-ordered surface is

$$\frac{d\sigma}{d\Omega}=\frac{4\pi^2 r_0^2 A}{\Gamma^2}\sum_{\tau_x,\tau_y}\delta(Q_x-\tau_x)\delta(Q_y-\tau_y)|F(\mathbf{Q})|^2 \times\left|\sum_{n=0}^{\infty}\rho_{\mathbf{Q}}(n)e^{iQ_z d_n}e^{-W_n(Q)}\right|^2 , \tag{4}$$

where A is the illuminated area, Γ is the area of the two-dimensional unit cell, and $F(\mathbf{Q})$ is the atomic form factor. $W_n(\mathbf{Q})$ is the Debye-Waller factor for the nth layer and d_n is the coordinate of the nth layer normal to the surface. τ_x and τ_y correspond to periodicities parallel to

the surface plane, and

$$\rho_{\mathbf{Q}}(n)=\sum_m \exp(i\tau_x x_{n,m}+i\tau_y y_{n,m}+iQ_z\Delta z_{n,m}) \quad (5)$$

is the amplitude of that density wave in the nth layer. In Eq. (5), $x_{n,m}$ and $y_{n,m}$ are atomic positions within the two-dimensional unit cell in the nth layer, and $\Delta z_{n,m}$ is the deviation of the mth atom in the nth layer from its ideal, bulk position in the direction normal to the surface.

When the diffractometer is set to accept a particular τ_x, τ_y, and Q_z, using Eq. (4) in Eq. (2), we find that

$$n_s/n_i=\frac{4\pi^2 r_0^2 A}{\Gamma^2 A_0}|F(\mathbf{Q})|^2\left|\sum_{n=0}^{\infty}\rho_{\mathbf{Q}}(n)e^{iQ_z d_n}e^{-W_n(\mathbf{Q})}\right|^2 \times L_0(\Delta Q_z/\Delta\theta_1)\ , \quad (6)$$

where ΔQ_z is the range of Q_z that falls within the diffractometer acceptance, and $L_0=(k^3\sin 2\theta)^{-1}$ is the Lorentz factor. ΔQ_z can be limited either by the in-plane collimation ($\Delta\theta_1$ and/or $\Delta\theta_2$), or in the case of nonspecular measurements at small incidence angles, by the out-of-plane acceptance ($\Delta\psi_2$). It is possible to require that the angle of incidence (α) and the angle of exit be equal to each other. Then, at large incidence angles,

$$\Delta Q_z=2k\Delta\theta_1\cos\theta\sin\theta/\sin\alpha\ ,$$

provided that the longitudinal resolution is determined by $\Delta\theta_1$ (and not by $\Delta\theta_2$) as is the case in the present experiments.[33,34] At large incidence angles it is straightforward to ensure that all of the x rays passed by slits in front of the sample are incident on the sample, so that $A/A_0=1/\sin\alpha$, and Eq. (6) becomes

$$n_s/n_i=\frac{4\pi^2 r_0^2}{\Gamma^2 k^2\sin^2\alpha}|F(\mathbf{Q})|^2\left|\sum_{n=0}^{\infty}\rho_{Q}(n)e^{iQ_z d_n}e^{-W_n(\mathbf{Q})}\right|^2 . \quad (7)$$

According to Eq. (7), the reflectivity (n_s/n_i) need not depend on the instrumental parameters, so that absolute measurements are possible.[35]

Near glancing incidence, $\Delta\mathbf{Q}_z=k\Delta\psi_2/\cos\alpha$ and

$$n_s/n_i=\frac{2\pi^2 r_0^2}{\Gamma^2 k^2\cos\alpha\sin\theta\cos\theta}\left[\frac{A}{A_0}\right]|F(\mathbf{Q})|^2 \times\left|\sum_{n=0}^{\infty}\rho_{Q}(n)e^{iQ_z d_n}e^{-W_n(\mathbf{Q})}\right|^2(\Delta\psi_2/\Delta\theta_1)\ , \quad (8)$$

which depends on the ratio $\Delta\psi_2/\Delta\theta_1$. In this case, it is difficult to prevent spillover of the incident beam because of the finite divergence of the x-ray source in the out-of-plane direction ($\Delta\psi_1$). Therefore, A is limited by the sample dimensions.

For the case of scattering from a single monolayer, an important consideration is the extent to which diffuse scattering from the bulk masks the surface signal. In the one-phonon approximation, the contribution of thermal vibrations to the cross section may be written[36]

$$\frac{d\sigma}{d\Omega}=Nr_0^2|F(\mathbf{Q})|^2e^{-2W(Q)}\sum_s\frac{k_BT}{M\omega_s^2(\mathbf{Q})}[\mathbf{Q}\cdot\mathbf{e}_s(\mathbf{Q})]^2\ . \quad (9)$$

M is the mass of a gold atom, $W(\mathbf{Q})$ is the bulk Debye-Waller factor, $\omega_s(\mathbf{Q})$ is the dispersion relation of the sth phonon branch, and $\mathbf{e}_s(\mathbf{Q})$ is its eigenvector. N is the number of atoms in the scattering volume. We may write $N=A\Lambda\rho_0/2$, where A is the illuminated area and ρ_0 is the number density. The penetration depth Λ depends on the angle of incidence (α) according to $\Lambda=\Lambda_0\sin\alpha$, where Λ_0 is the attenuation length. From Eq. (3) we, therefore, find

$$n_s/n_i=\tfrac{1}{2}\Lambda_0\rho_0 r_0^2|F(\mathbf{Q})|^2e^{-2W(\mathbf{Q})} \times\sum_s\frac{k_BT}{M\omega_s^2(\mathbf{Q})}[\mathbf{Q}\cdot\mathbf{e}_s(\mathbf{Q})]^2\Delta\Omega\ , \quad (10)$$

independent of α. This can be contrasted with Eq. (7), where n_s/n_i falls off as $(\sin\alpha)^{-2}$. Therefore, at sufficiently large α, the bulk thermal diffuse scattering overwhelms the surface signal. The contribution from thermal vibrations, at grazing incidence, is

$$n_s/n_i=\tfrac{1}{2}\Lambda_0\rho_0\left[\frac{A\sin\alpha}{A_0}\right]r_0^2|F(\mathbf{Q})|^2e^{-2W(\mathbf{Q})} \times\sum_s\frac{k_BT}{M\omega_s^2(\mathbf{Q})}[\mathbf{Q}\cdot\mathbf{e}_s(\mathbf{Q})]^2\Delta\Omega\ , \quad (11)$$

which depends linearly on $\sin\alpha$. In the Appendix we show that thermal diffuse scattering accounts both for the magnitude of the background in these experiments and for its $\mathbf{Q}$ dependence, except at small scattering angles.

Because of the phenomenon of total external reflection, all of our expressions for n_s/n_i are modified by a factor $|T(\alpha)|^4$, where $T(\alpha)$ is the Fresnel (amplitude) transmission coefficient.[37] (This form follows when the angles of incidence and exit are held equal.) However, $T(\alpha)$ differs appreciably from unity only for incidence angles less than or of the order of the critical angle ($\alpha_c\cong 0.45°$ at $E=10$ keV). Also, for $\alpha<\alpha_c$, the x-ray penetration depth is significantly reduced from the simple result given above and the scattering from bulk thermal vibrations is much reduced.

C. Experiment

The experiments described in this paper were carried out using Beamline X20A at the National Synchrotron Light Source (NSLS). Approximately 4 mrad of synchrotron radiation from a bending magnet were collected and focused by a platinum-coated, bent, cylindrical, float-glass mirror. Monochromatic x rays of energy $E=10$ or 10.5 keV were selected by a pair of perfect Si(111) or Ge(111) crystals. At the sample position, we obtained on the order of 3×10^{11} photons in a bandwidth $\Delta E/E=2\times10^{-4}$ and a spot size approximately 1.0×0.5 mm^2. The incident x-ray collimation was determined by the vertical angular divergence of the source ($\Delta\theta_1\cong 0.2$ mrad) and the horizontal acceptance of the mirror

($\Delta\psi_1 \cong 4$ mrad).

The experiments were performed using a four-circle diffractometer[38] with a vertical scattering plane. For the glancing incidence measurements ($\alpha = 0.2°$), a large (80×30 mm^2) perfect Ge(111) crystal was employed as an analyzer crystal on the detector arm to provide fine resolution within the scattering plane ($\Delta\theta_2 = 0.1$ mrad acceptance). Slits were used to define the out-of-plane acceptance ($\Delta\psi_2 = 20$ mrad). At glancing incidence, the diffuse direction of the cross section [Eq. (7)] is matched to the large out-of-plane acceptance, while the in-plane resolution is uncompromised. This is the principal advantage of the glancing incidence geometry. The fine-resolution measurements described in Secs. III B and III C were carried out mainly at wave-vector transfers near 2.5 Å^{-1}, where the radial resolution is $\Delta Q_r \cong 0.0009$ Å^{-1} full width at half maximum (FWHM) and the transverse resolution is $\Delta Q_\eta \simeq 0.0002$ Å^{-1} FWHM.[39] For the reflectivity measurements which were performed with larger incidence angles, slits were used to determine both the in-plane acceptance ($\Delta\theta_2 = 2$ mrad) and the out-of-plane acceptance ($\Delta\psi_2 = 10$ mrad).

Two different gold samples were used in these experiments. They were cut from the same boule at Oak Ridge National Laboratory (ORNL), where the sample characterization was performed. Initial sample heating resulted in segregation of Ca to the surface, forming localized Ca deposits, as revealed by scanning electron microscopy and electron-induced x-ray fluorescence. After cleaning by Ar^+ ion bombardment and annealing, no Ca was detected by Auger electron spectroscopy (AES); in addition, the low-energy-electron-diffraction (LEED) pattern reproduced earlier results in detail.[2] Following prolonged periods at elevated temperatures, trace amounts of Ca became observable in AES, but were readily removed by sputtering.

For the x-ray diffraction experiments reported here, the sample was contained within a small vacuum chamber[34,40] which mounts directly onto a Huber six-circle diffractometer.[41] Sample heating was provided by a small potted heater. The sample temperature was monitored by means of a Chromel-Alumel thermocouple and by direct measurement of the gold lattice constant. The pressure in the chamber was typically 3×10^{-9} Torr, while the sample was held at elevated temperatures. During the experiment, clean surfaces were periodically prepared by Ar^+ ion bombardment (500 V and 1 μA). Previous experience with x-ray experiments on the Au(001) surface has shown that results obtained on gold surfaces prepared and studied in this way are identical to those obtained when demonstrably clean gold surfaces are studied in an x-ray diffraction chamber with *in situ* AES.[40] As in our earlier experiments on gold surfaces,[34,40] the bulk mosaicity of the sample was improved from $\cong 0.2°$ to $\cong 0.02°$ by annealing at high temperatures (1250 K). The x-ray measurements presented in Sec. III were obtained for several cycles of the temperature, both increasing and decreasing. At each temperature, the sample was allowed to equilibrate for at least 30 min before measurements were performed. The x-ray diffraction pattern was found to be reproducible for extended periods and from one sample to the other. After the x-ray measurements, the samples were returned to ORNL and, after routine cleaning and annealing, again yielded the expected LEED pattern at 300 K.[2]

III. RESULTS AND DISCUSSION

A. Specular and nonspecular reflectivity

In this section we present measurements of the absolute x-ray reflectivity of the Au(111) surface for temperatures between 300 and 1250 K. Both the specular and nonspecular reflectivities are described. At all temperatures, nonzero reflectivity was observed only along directions perpendicular to the crystallographic cubic (111) planes of the bulk. This indicates that on length scales up to 5000 Å the surface is perfectly aligned with the cubic (111) planes.[42] This is expected from high-temperature studies of gold equilibrium crystal shapes,[43] which show that there is a range of forbidden surface orientations both near the cubic [111] and [001] directions. We therefore believe that any small, macroscopic, surface misalignment from the cubic (111) planes plays no role in these experiments. Presumably, the development of large (111) facets results from annealing at high temperatures, where surface diffusion rates are high. We have observed similar behavior in our studies of Au(001) surfaces.[40]

The absolute x-ray reflectivity at 300 K measured through a number of bulk Bragg peaks is shown in Fig. 2 plotted on a logarithmic scale. Each profile corresponds to a different in-plane wave vector. Sharp peaks locate bulk Bragg reflections. The spacing between Bragg reflections in a given profile is $\Delta L = 3$, but they occur at different values of L for different in-plane wave-vector transfers. The dashed line is the reflectivity expected for an unreconstructed, unrelaxed surface (ideal termination). By unrelaxed, we mean that the interlayer spacings between near-surface layers are unchanged from those in the interior. An unreconstructed surface is one for which the in-plane symmetry and lattice constants are identical to that of a bulk plane. For the measurements reported in this section, the detector acceptance was determined by slits ($\Delta\theta_2 = 2$ mrad, $\Delta\psi_2 = 10$ mrad). Each data point (open and solid circles) corresponds to the integrated intensity obtained by rocking the crystal through the reflection condition [Eq. (4)]. Thermal diffuse scattering from the bulk was subtracted in all cases (see the Appendix). The data have been placed on an absolute scale [Eq. (7)] by comparison with the intensity near the bulk Bragg reflections. This is possible because the integrated intensities near Bragg reflections depend only on the atomic form factor of gold and on the amplitude of atomic vibrations in the bulk (Debye-Waller factor), which are well established. Therefore, they may be used to normalize all of the data to the incident flux.

In reference to Fig. 2, the measured reflectivity increases rapidly near the bulk Bragg peaks. [For example, see Fig. 2(a) at $L = 3$ and 6 for the specular reflectivity and Fig. 2(b) at $L = 2$ and 5 for the nonspecular reflectivity along $(0,1,L)$.] Between bulk Bragg peaks the reflectivity is much reduced and depends sensitively on the details of the surface structure. Noteworthy in Fig.

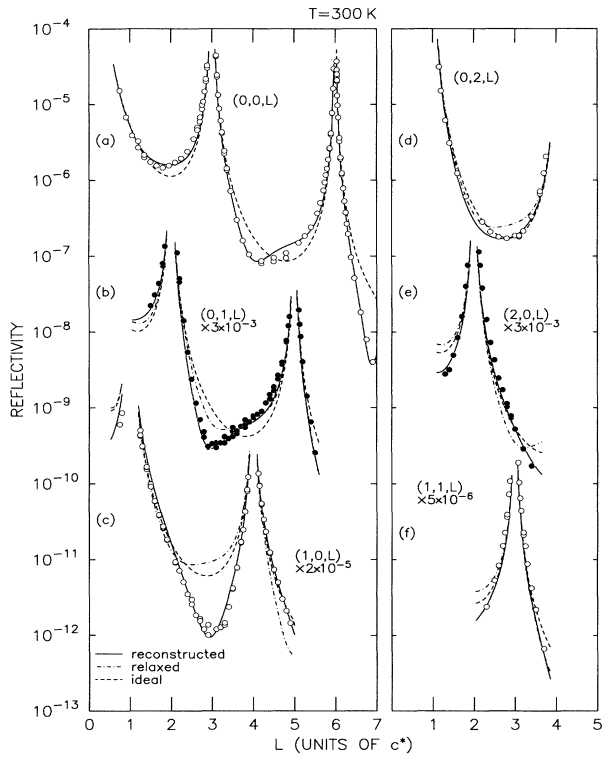

FIG. 2. Au(111) reflectivity for various in-plane bulk periodicities vs momentum transfer normal to the surface (L) at 300 K. Reflectivity for three different models of the surface structure are shown as the solid, dashed, and dot-dashed lines. The models are discussed in the text. (a) The specular reflectivity. (b), (c), (d), (e), and (f): Nonspecular reflectivity. The minima at $L=3$ in (b) and (c) are due to interference between x rays scattered by surface atoms in C-stacking and A-stacking sites.

2(a) is the slight asymmetry of the specular reflectivity about the (0,0,3) Bragg peak and the more pronounced asymmetry about the (0,0,6) Bragg peak relative to the reflectivity expected for ideal termination (dashed lines). It has been shown previously[34,40] that an expansion of the spacing between the top and second layers (d_{01}) gives rise to a specular profile of just this character. Another important feature of the data shown in Fig. 2 is the presence of pronounced dips in the nonspecular reflectivity of Figs. 2(b) and 2(c), between the bulk Bragg peaks ($L=3$).

Figure 2(a) shows the specular reflectivity, extending continuously from near the origin of reciprocal space and through the (0,0,3) and (0,0,6) bulk Bragg reflections [the cubic (1,1,1) and (2,2,2), respectively]. This corresponds to a range of wave-vector transfer perpendicular to the surface extending from $Q_z=0.7$ to 6.2 Å^{-1}. The reflectivity expected for an unreconstructed, unrelaxed Au(111) surface (dashed lines) does not provide an adequate description of the measured specular reflectivity. The solid lines in Fig. 2 are the results of the best fit of all of the reflectivity profiles measured at 300 K to a simple model of the reconstruction, which allows for an expansion or contraction of d_{01} and d_{12}, for a surface-normal root-mean-square (rms) displacement amplitude in the near-surface layers (σ_n) and includes two excess atoms within a $(s\times\sqrt{3})$ unit cell (with $s=23$). Both atomic vibrations normal to the surface and any surface corrugation are subsumed into the rms displacement amplitude.[40] For the specular reflectivity, the model [Eq. (7)] reduces to

$$n_s/n_i=\frac{4\pi^2r_0^2}{\Gamma^2k^2\sin^2\alpha}|F(\mathbf{Q})|^2\left|\sum_{n=0}^{\infty}\rho_0(n)e^{iQ_zd_n-\sigma_n^2Q_z^2/2}\right|^2, \tag{12}$$

with $d_{01}=d_0-d_1$ and $d_{12}=d_1-d_2$, and $\rho_0(0)=\frac{24}{23}=1.0435$ and $\rho_0(n)=1$ for $n\geq 1$. For these fits the parameters allowed to vary were the interlayer spacings near the surface (d_0 and d_1) and the surface-normal rms displacement amplitudes. The top layer density was fixed at $\rho_0(0)=\frac{24}{23}=1.0435$. We did perform fits, however, of the specular reflectivity allowing the top layer density to vary. These fits converge to a top layer density $\rho_0(0)=1.03\pm0.04$. The best-fit values of d_{01} and d_{12} are reliably determined by the specular reflectivity because it does not depend explicitly on the atomic coordinates within the plane of the surface. In this case, we find a value for d_{01} which corresponds to a $3.3\pm0.4\%$ expansion relative to the bulk (111) interlayer spacing. The best-fit value of d_{12} corresponds to a $0.8\pm0.4\%$ contraction. The excess areal density of the reconstructed layer [1.0435 times that of bulk (111) planes] together with the 3.3% expansion imply that the volume density in the surface selvedge is slightly increased relative to that in the bulk.[34,40] As for the displacement amplitudes, only that in the top layer is significantly different from the value expected from bulk thermal vibrations. This is consistent with the small surface corrugation observed by STM (Ref. 9) and He diffraction[7] and a slight enhancement of the surface vibrational amplitude.

The nonspecular reflectivities cannot be understood solely on the basis of surface relaxation. For these profiles [Figs. 2(b)–2(f)], there is a component of the wave-vector transfer parallel to the surface. They are therefore sensitive to atomic coordinates within the plane of the surface. In particular, the pronounced dips in the profiles of Figs. 2(b) and 2(c) result from the ABC-to-ABA faulting.[44] [The dash-dotted lines of Figs. 2(b)–2(f) show the reflectivity expected for a relaxed surface with no stacking faults.] Motivated by Refs. 7 and 9, we have parametrized the model stripe-domain structure as follows. We assume a rectangular $(23\times\sqrt{3})$ unit cell for a single, reconstructed, surface layer (Fig. 3). Within that unit cell, there are two excess gold atoms, corresponding to an increased areal density of the top layer by a factor of $\frac{24}{23}=1.0435$. This is consistent with the specular reflectivity. Initially, atoms within the unit cell are uniformly spaced, but we allow for discommensurations by including the possibility of additional displacements, as follows. In our model unit cell, the first atom is located at a C site, but then the displacement pattern in the 23-fold direction (x direction) is described by a sine series and in the $\sqrt{3}$-fold direction (y direction) by a cosine series. Explicitly, the fractional coordinates of the mth

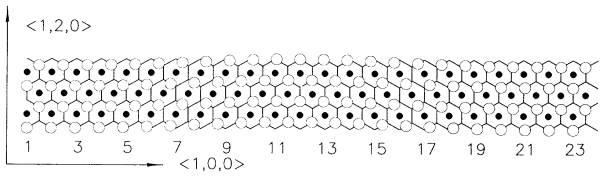

FIG. 3. Discommensuration structure of the Au(111) surface. Solid circles represent the in-plane positions of second layer atoms in B sites. Hatched circles represent the positions of the surface layer atoms determined by the best fit to the reflectivity at 300 K. The displacement from C sites to A sites is best viewed by looking in the $\langle 1,0,0\rangle$ direction at low angles to the page.

atom in the $23\times\sqrt{3}$ unit cell are given by

$$x_m = -m/23 + \frac{a_1}{2\pi}\sin(2\pi m/23) + \frac{a_2}{2\pi}\sin(4\pi m/23) + \cdots ,$$

$$y_m = b_1[1-\cos(2\pi m/23)]/4\sqrt{3} + b_2[1-\cos(4\pi m/23)]/4\sqrt{3} + \cdots .$$

The amplitude of each Fourier component $(a_1, a_2, \ldots, b_1, b_2, \ldots)$ is a possible independent fitting parameter. In the calculations, the reflectivities of each of the three possible orientations of the $(23\times\sqrt{3})$ structure have been added together incoherently.

The solid lines of Fig. 2 correspond to the best-fit parameters. It is clear that this model provides an excellent description of all of the data. Firstly, note that the fitted displacements in the $\sqrt{3}$ direction are such that atoms at the center of the unit cell are located at faulted A sites. The best-fit parameters ($a_1 = 0.312\pm0.03$, $a_2 = 0.022\pm0.002$, $b_1 = 1.009\pm0.1$, $b_2 = -0.151\pm0.02$) give rise to displacements in the $\sqrt{3}$ direction at the center of the unit cell of 0.84 ± 0.12 Å. For comparison, a displacement of 0.83 Å is necessary to place the atoms at A sites. To establish that the faulted regions are indeed ABA stacking regions, both the $(1,0,L)$ and the $(2,0,L)$ profiles are important in that with any significant deviation from ABA stacking either the $(1,0,L)$ or the $(2,0,L)$ model profile ceases to provide a good description of the data. Secondly, it is worth noting that to obtain the fits shown in Fig. 2, only two terms in each of the sine and cosine series were required. In addition, the amplitude of the second harmonic is significantly smaller than that of the first harmonic in both cases: Specifically, for displacements in the 23-fold direction the ratio of the second harmonic to the first is 0.07, and in the $\sqrt{3}$-fold direction it is 0.15. Including higher harmonics did not improve the quality of the fit. Thus, the displacement field associated with the discommensurations is essentially sinusoidal.[17] The $(23\times\sqrt{3})$ unit cell obtained with our best-fit parameters is illustrated in Fig. 3. The A and C sites are located at the vertices of the hexagonal lattice. It is evident from the figure that atoms in the reconstructed layer are confined to positions along the sides of the hexagons (bridge sites). By assigning atoms closer to C sites to an unfaulted region and atoms closer to A sites to a faulted region, we have determined the ratio of the sizes of faulted to unfaulted regions to be 0.7. This is in agreement with the results of He atomic beam diffraction[7] and STM (Ref. 17) studies.

Figure 4 shows the reflectivity obtained at three different temperatures: 300 K (open circles, reproducing some of the profiles of Fig. 2), 750 K (solid squares), and 1200 K (open triangles). It is clear that the data exhibit the same general features at each temperature although at high temperature the reflectivity between Bragg peaks, especially at large L, is somewhat reduced. The reflectivity cannot be described by a relaxed or unreconstructed surface, implying that the surface is reconstructed for all temperatures between 300 and 1200 K. Furthermore, the similarity of the data at these three different temperatures suggests that the basic picture involving faulted and unfaulted surface regions remains correct throughout this temperature range. To test this idea, we performed fits for which the Fourier coefficients

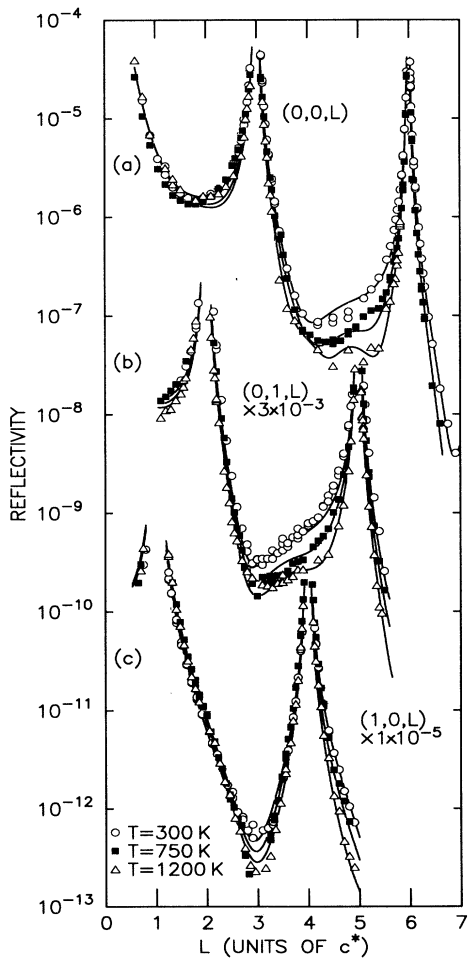

FIG. 4. Reflectivity profiles for various in-plane, bulk periodicities as a function of momentum transfer normal to the surface (L) at three temperatures. The open circles, solid squares, and open triangles correspond to 300, 750, and 1200 K, respectively. The solid lines are best fits to the reconstruction model.

describing the in-plane structure were fixed at their room-temperature, best-fit values. The amplitudes of the surface-normal vibrations and the spacings between near-surface layers (d_{01} and d_{12}) were then allowed to vary. The solid lines in Fig. 4 are the model profiles which result. As may be seen, the model describes the data very well. Quantitative results from the fits are shown in Fig. 5. Figure 5(b) shows the fractional change in the spacing between near-surface layers from the bulk (111) interlayer spacing (relaxation) versus temperature. The magnitudes of d_{01} and d_{12} both appear to decrease slightly with increasing temperature, though the apparent change is smaller than the error of our measurements. Figure 5(a) shows the best-fit values of the surface-normal displacement amplitudes. Compared to the crystal interior, the displacement amplitudes are significantly enhanced near the surface, decaying to the bulk value within a few layers.[27] To obtain the fits shown in Figs. 2 and 4, it was not necessary to allow for enhanced vibrational amplitudes within the plane of the surface. Nor was it necessary to consider the possibility that two layers participate in the reconstruction, as suggested in Ref. 7.

We should emphasize that in the present section, we have examined the reflectivity obtained only at bulk periodicities. While we have assumed a $(23\times\sqrt{3})$ unit cell in the analysis, it is not possible to establish a specific structural model for the reconstruction on the basis of bulk reflectivity alone. However, we believe that the analysis demonstrates that the structure is composed of faulted and unfaulted regions throughout the temperature range studied. In Sec. III B, where measurements of the in-plane diffraction pattern are described, we will show how the basic $(23\times\sqrt{3})$ motif fits into the structure of the chevron phase.

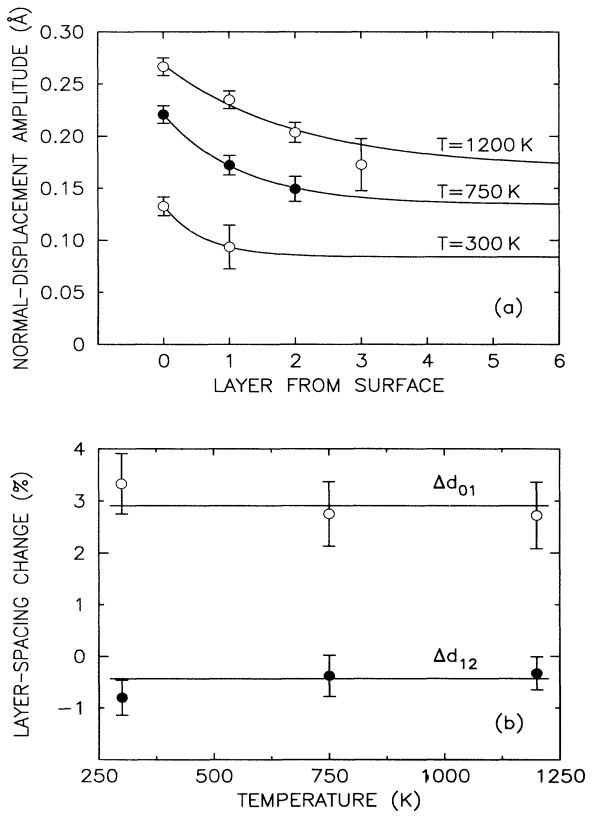

FIG. 5. Results of fits to the reflectivity as a function of temperature. (a) Fitted values of the surface-normal root-mean-square displacement amplitude vs layers from the surface. (b) Fitted values of the interlayer spacing change vs temperature.

B. Chevron phase

In this section we present measurements of the in-plane diffraction pattern of the reconstructed Au(111) surface in the temperature range between 300 and 865 K. We will show that the existing structural model for the Au(111) surface is incomplete and must be extended to incorporate an equilibrium density of well-ordered kinks between two of the three possible orientational domains of the $(s\times\sqrt{3})$ discommensuration structure ($s\cong 23$). Because of the resultant zig-zag pattern of discommensurations, we call this phase the chevron phase. Firstly, we describe the evidence for a chevron structure at 300 K. Then follows a discussion of its behavior as a function of temperature. We will show that the apparently complicated temperature evolution of the diffraction pattern between 300 and 865 K can be readily explained in terms of the chevron structure. Finally, we present data that demonstrate that the chevron reconstruction is confined to the surface layer.

Unless otherwise stated, the scans presented in this section were all obtained at glancing incidence ($L=0.12$, $\alpha=0.2°$) in the neighborhood of the $(0,1,L)$ bulk rod using a Ge(111) analyzer crystal on the detector arm to provide fine resolution. However, scans were also taken in the neighborhood of the $(0,2,L)$ bulk rod at $L=0.12$ and near $(0,1,L)$ at different values of L to verify our conclusions.

By way of introduction, Fig. 6(a) shows the HK plane of reciprocal space for the Au(111) surface in the hexagonal coordinate system. Open circles in Figs. 6(a)–6(c) represent lateral periodicities of the bulk crystal (truncation rods). The small hexagon drawn about the $(0,1,L)$ rod in Fig. 6(a) is reproduced in detail in Figs. 6(b) and 6(c). Solid symbols surrounding each truncation rod in Figs. 6(a)–6(c) arise from the reconstruction (surface rods). The diffraction pattern expected from a single orientational domain of the striped phase is shown in Fig. 6(a) and that expected for the stripe-domain structure with all three orientational domains present is shown in Fig. 6(b). We have used different symbols (solid circles, squares, and triangles) to distinguish scattering from the three distinct, rotationally equivalent domains. In Fig. 6(b), the positions of peaks corresponding to the surface reconstruction are displaced from the bulk truncation rod by $\delta_D=2\pi/L_D$, where L_D is the period of the discommensuration structure. The scattering from the three rotationally equivalent domains of the reconstruction is assumed to add incoherently.

Figure 7 shows a series of scans obtained at 300 K in the neighborhood of the $(0,1,L)$ rod. Figure 6(c) indicates the paths in reciprocal space followed for each scan

(the dot-dashed lines) and summarizes the observed diffraction pattern. Thus, with reference to Fig. 7 (i) and (iii) are scans along the sides of the elementary hexagon of Fig. 6(c), while (ii) and (iv) are scans across the center of that hexagon. The strong peak at the center of scans (ii) and (iv) is the bulk $(0,1,L)$ rod. Peaks may also be discerned at the center of (i) and (iii), although they are much weaker. Displaced from each central peak, there are still more peaks. In the figure the vertical dashed lines indicate multiples of a fixed separation from the central component. It is clear that many of the observed peaks can be categorized on this basis and correspond, therefore, to a fundamental, new incommensurability of the Au(111) surface (δ_K). These peaks [especially those in scans (i) and (iii)] are, however, broader than can be accounted for from consideration of the spectrometer resolution and sample mosaic. Additional features, which are indicated by arrows in Fig. 7, occur at the vertices of the hexagon of Fig. 6(c) and correspond to the overlaps of each scan with the tails of the peaks that occur along the other sides of the hexagon. In this context, we note that the separation of the peaks at $\eta \cong \pm 0.04$ from the bulk rod at $\eta = 0$ in Fig. 7 (iv), equals the discommensuration wave vector (δ_D) at 300 K. Hence, we find that the unit cell of the reconstructed Au(111) surface is characterized by two incommensurate wave vectors, δ_K and δ_D. At 300 K, δ_K is close to $0.2\delta_D$.

The difference between the observed diffraction pattern [Fig. 6(c)] and that illustrated in Fig. 6(b) requires a more elaborate surface structure than the $(s \times \sqrt{3})$ reconstruction proposed in earlier work.[1-10] It seems clear, however, that the $(s \times \sqrt{3})$ motif is an essential component of the Au(111) surface structure. Therefore, it is natural to consider a structure involving an ordered array of defects separating rotationally equivalent domains of the $(s \times \sqrt{3})$ reconstruction. The simplest realization of this idea is a kink, as illustrated in Fig. 6(d). A periodic array of kinks separating two of the three possible orientational domains—the chevron structure—produces a surface structure with unit-cell dimensions L_K along the $\langle 1,0,0 \rangle$ directions, where L_K is twice the separation between neighboring kinks, and $2L_D/\sqrt{3}$ along the $\langle 1,2,0 \rangle$ directions. The corresponding diffraction pattern consists of peaks separated by $\delta_K = 2\pi/L_K$ along $\langle 2,\bar{1},0 \rangle$, and by $\sqrt{3}\delta_D/2$ along $\langle 0,1,0 \rangle$. The observed diffraction pattern [Fig. 6(c)] can be understood on this basis, provided that scattering from all three orientationally equivalent domains of the chevron reconstruction is included. It is

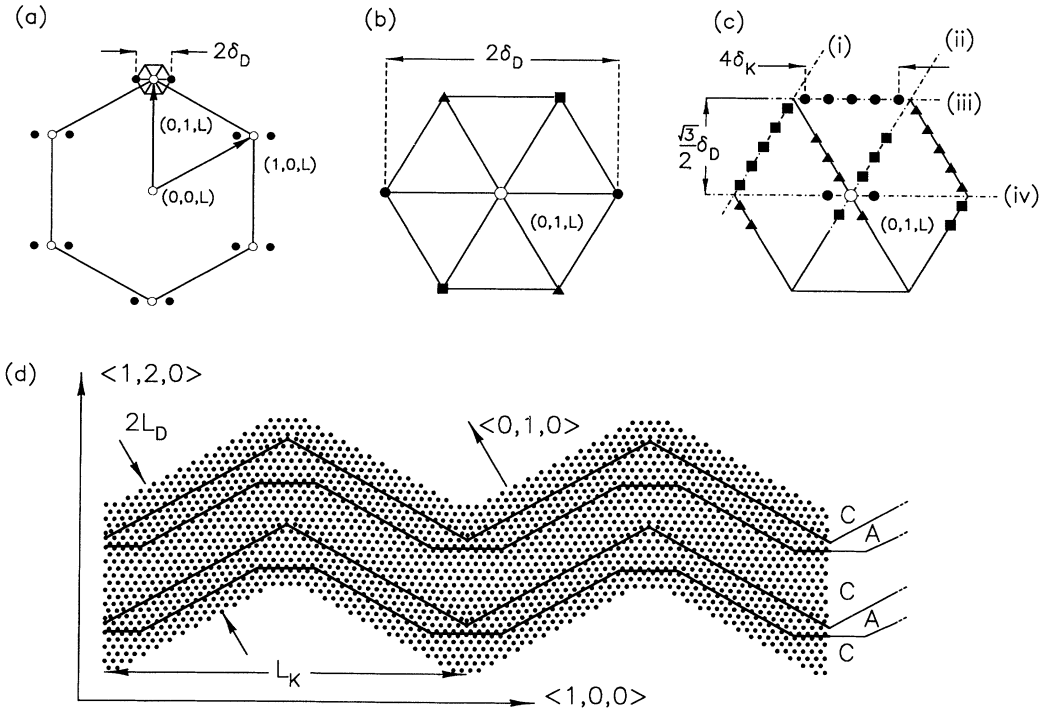

FIG. 6. Schematic of reciprocal space for the Au(111) surface. In (a), (b), and (c) the open circles correspond to bulk in-plane periodicities and the solid symbols correspond to reconstruction peaks. (a) Diffraction pattern expected from a single domain of the discommensuration structure. The small hexagon about the $(0,1,L)$ position has been reproduced in detail in (b) and (c). (b) Diffraction pattern expected for the Au(111) surface with three rotationally equivalent discommensuration domains. (c) Schematic of the observed diffraction pattern in the vicinity of the $(0,1,L)$ rod. Different solid symbols correspond to scattering from different rotational domains of the chevron phase. Labels (i), (ii), (iii), and (iv) indicate different scan directions presented in Fig. 7. (d) Four unit cells of the chevron structure. Zig-zag lines and the capital letters on the right indicate surface regions with the correct fcc stacking (C) and the faulted (A) stacking. For clarity, the $(s \times \sqrt{3})$ discommensuration structure and consequently the kink structure have been scaled in size to that $s = 9$ for the chevrons plotted in (d).

noteworthy that no peak appears at the hexagonal vertices, in contrast to the diffraction pattern for the $(s\times\sqrt{3})$ structure. To establish definitively by x-ray diffraction that the discommensurations are arranged in a chevron pattern requires that the experimentally observed intensities be reproduced by this model. We will show below that there is good agreement. We believe that the differences between our diffraction pattern and those obtained with electron[1-5] or atom[7] scattering are a result of the finer reciprocal space resolution possible with synchrotron x-ray scattering.

We now turn to a description of the temperature dependence of the diffraction pattern by focusing on profiles transverse to the K direction through $(0,1+\sqrt{3}\delta_D/2,0.12)$. This corresponds to the path labeled (iii) in Fig. 6(c). Results of representative scans at several temperatures between 300 and 865 K are shown in Fig. 8. Each profile consists of a number of closely spaced peaks. With increasing temperature, the peak separation (δ_K) increases and a complicated evolution of the relative intensities and widths occurs. At 300 K [Fig. 8(a)], the peak at $\eta=0$ is very weak and the stronger peaks at $\eta=\pm\delta_K$ and $\eta=\pm2\delta_K$ are relatively broad compared to equivalent peaks at higher temperatures. Also evident is that the widths of the peaks at $\eta=\pm2\delta_K$ are broader than those at $\eta=\pm\delta_K$ [half width at half maximum (HWHM)$=0.0026a^*$ for $\eta=\pm2\delta_K$ versus HWHM$=0.0009a^*$ for $\eta=\pm\delta_K$]. There are broad shoulders near $\eta=\pm3\delta_K$ but they are too broad and weak to be resolved as distinct peaks at 300 K. At 590 K [Fig. 8(b)], the peaks at $\eta=0$ and $\eta=\pm3\delta_K$ are more intense than at 300 K. In contrast, at 750 K [Fig. 8(c)] the peaks at $\eta=0$ and $\eta=\pm3\delta_K$ are much weaker. Furthermore, the value of δ_K has increased relative to its value at 590 K. At 800 K [Fig. 8(d)], δ_K has increased still further and the peaks are noticeably narrower. The peak at $\eta=0$ regains considerable intensity, while those at $\eta=\pm3\delta_K$ are no longer visible. By 850 K, the peak at $\eta=0$ has further intensified and those at $\eta=\pm2\delta_K$ have become much weaker.

To extract reliable peak intensities, positions, and widths, we have fit the transverse scans of Fig. 8 and those obtained at intermediate temperatures to a model composed of five Lorentzians. The amplitude and width of each was an independent fitting parameter. However,

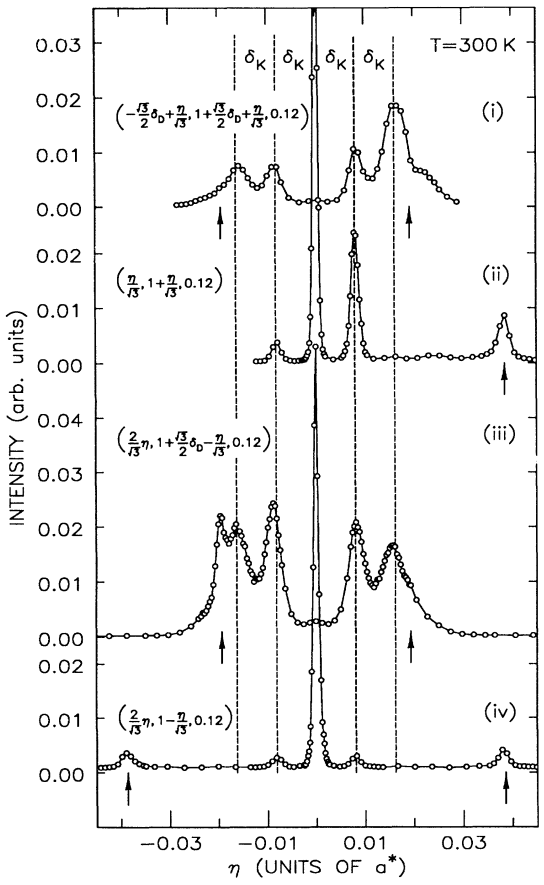

FIG. 7. High-resolution glancing angle scans through reconstruction peaks in the vicinity of (0,1,0.12). The different scan directions, (i), (ii), (iii), and (iv) are displayed in Fig. 6(c).

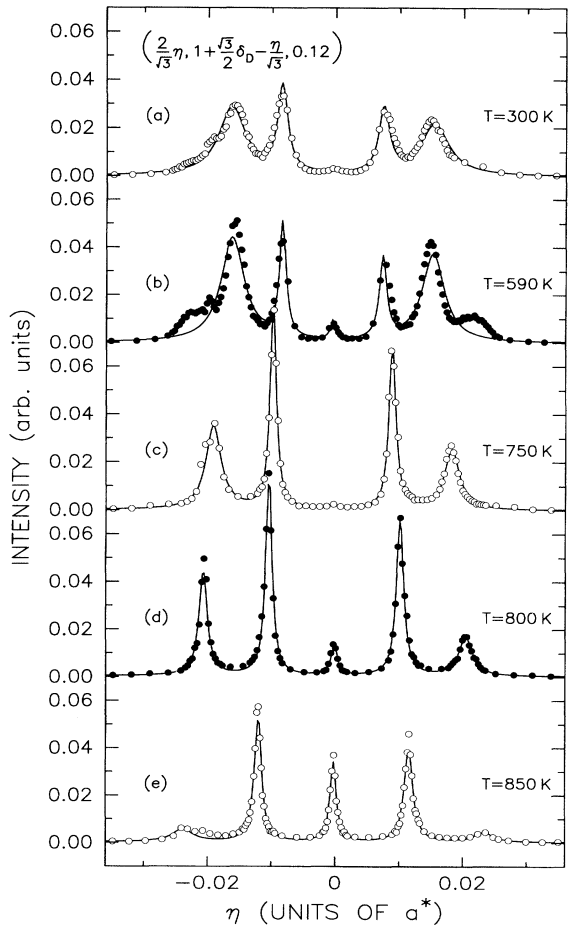

FIG. 8. Scans transverse to $(0,1+\sqrt{3}\delta_D/2,0.12)$ as a function of temperature, i.e., along the path labeled (iii) in Fig. 6(c). The peaks are separated by the kink wave vector, δ_K. Transverse scans at (a) 300, (b) 590, (c) 750, (d) 800, and (e) 850 K. The solid lines are best fits as discussed in the text.

the peak positions were constrained to be equally spaced. The resultant best-fit model profiles are shown as solid lines in Fig. 8. The model provides a reasonable description of the data, and the discrepancies are readily understood: The peak near $\eta \cong -0.02$ originates from a different rotational domain of the chevron structure [see Fig. 6(c)]. In addition, the model does not not account for all of the observed scattering at large displacements from $\eta=0$ which is the result of diffuse peaks at $\eta=\pm 3\delta_K$. The intensities of these features are too small and too near the other peaks to be sensibly included in the fit. Nevertheless, the model line shapes provide an accurate measure of the intensities, widths, and spacing of the peaks at $\eta=0, \pm\delta_K, \pm 2\delta_K$.

Figure 9 shows the temperature dependence of the two incommensurate wave vectors (δ_D and δ_K). Both wave vectors increase monotonically with increasing temperature, corresponding to a contraction of the unit cell relative to the bulk lattice spacing. However, while the average discommensuration periodicity varies smoothly from $L_D=22.5a$ at 300 K to $20.9a$ at 850 K, the average kink periodicity is essentially constant between 300 and 700 K ($L_K \cong 112.4a \cong 324.3$ Å). Beyond 700 K, the kink density increases rapidly, so that by the disordering transformation the kink periodicity has decreased by a factor of 1.6 to $L_K=70.4a=204.9$ Å. The ratio of δ_K over δ_D varies from $\cong 0.2$ at 300 K to $\cong 0.3$ at 850 K, as shown in Fig. 10.

Figure 11 displays the fitted HWHM in the transverse direction of the various peaks shown in Fig. 8 as a function of temperature. Widths of the peak at $\eta=0$ are shown as crosses, those of the peaks at $\eta=\pm\delta_K$ are shown as solid circles and solid squares, and those of the peaks at $\eta=\pm 2\delta_K$ are shown as open circles and open squares. The measured width of the central peak (crosses in Fig. 11) is entirely the result of the finite sample mosaic. The excess width of the other peaks arises because of positional disorder within the reconstructed layer. It is clear from Fig. 11 that the peaks corresponding to the

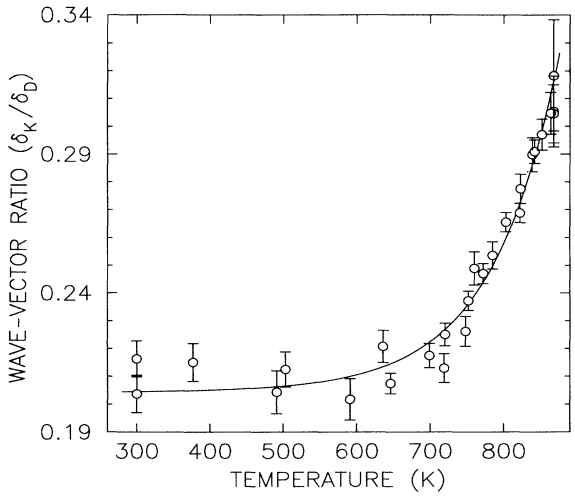

FIG. 10. Ratio of the kink wave vector to the discommensuration wave vector plotted as a function of temperature.

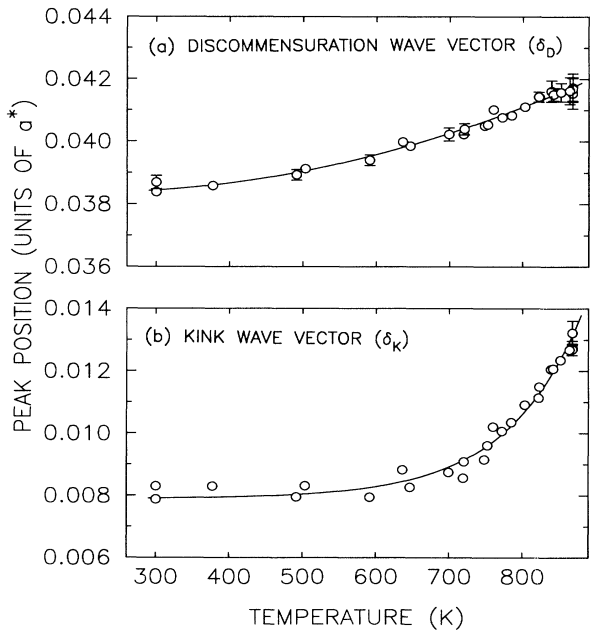

FIG. 9. Results of glancing angle measurements of surface reconstruction periodicities vs temperature. (a) Discommensuration wave vector vs temperature. (b) Kink wave vector vs temperature.

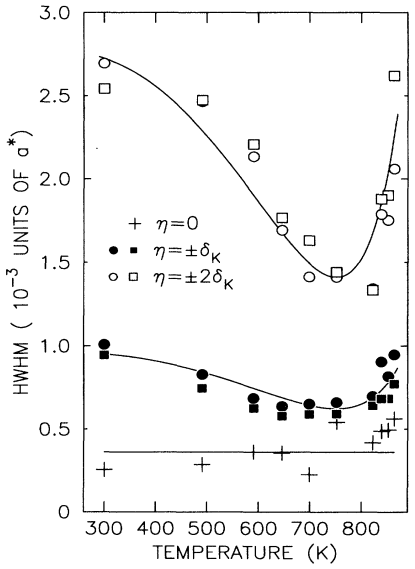

FIG. 11. Half widths at half maximum vs temperature for peaks transverse to $(0, 1+\sqrt{3}\delta_D/2, 0.12)$. Data for $\eta=0$ are plotted as crosses. Solid circles are the data for $\eta=\delta_K$ and solid squares are the data for $\eta=-\delta_K$. Open circles are the data for $\eta=2\delta_K$ and open squares are the data for $\eta=-2\delta_K$. Widths of the peak at $\eta=0$ are due to the sample mosaic. The excess width of the peaks at $\eta=\pm\delta_K$ and $\pm 2\delta_K$ is due to the rms fluctuation in L_K.

density wave at $2\delta_K$ are significantly broader than those for the density wave at δ_K. However, the temperature variation of the width of the peak at $2\delta_K$ mimics that at δ_K. In Fig. 11 the line through the widths of the peaks at $2\delta_K$ illustrates a factor of 4 larger excess width than does the line through the widths of the peaks at $\pm\delta_K$. Therefore, our data are consistent with an η^2 scaling. This would result if the distance between kinks were a Gaussian random variable with a variance that grows linearly with distance across the surface.[45] This observation provides an explanation of why the peaks at $\eta=\pm 3\delta_K$ are so broad (Fig. 8). Within the context of this model, the deconvolved HWHM (κ_m) for a Lorentzian peak at $\eta=\pm m\delta_K$ is given by $\kappa_m L_K = m^2\delta_K^2\sigma_K^2/2$, where σ_K is the root-mean-square fluctuation in L_K. At its minimum between 700 and 800 K, $\sigma_K \cong L_K \sqrt{(\kappa_m/\pi m^2\delta_K)} \cong 23$ Å; at 300 K, it is ~ 50 Å. The fluctuation in L_K is smallest when the ratio of the kink wave vector to the discommensuration wave vector is close to one-quarter. At one-quarter, the unit-cell dimensions are such that the distance along the $\langle 0,1,0\rangle$ directions (perpendicular to the discommensurations) between kinks exactly equals four complete discommensuration periods.

Figure 12(a) shows the temperature dependence of the integrated intensities. The intensities of the peak at $\eta=0$ are shown as the crosses, the intensities of the peaks at $\eta=\pm\delta_K$ are plotted as solid circles and solid squares, and the intensities of the peaks at $\eta=\pm 2\delta_K$ are plotted as open circles and open squares. Evident from these data is the change in the weight of the scattering from larger η towards small η with increasing temperature. In addition, it is striking that there is a minimum in the intensity of the central peak at approximately 730 K. To compare these data to a calculation of the intensities expected for the chevron structure, it is convenient to display them not as a function of temperature but rather as a function of δ_K/δ_D. This is shown in Fig. 12(b). The minimum in the intensity of the central peak ($\eta=0$) occurs at $\delta_K/\delta_D=0.22$ and the weight of the intensity shifts from larger η to smaller η as δ_K/δ_D increases. Our initial approach to understanding this behavior was to calculate the peak intensities on the basis of a chevron reconstruction with abrupt kinks between the different domains of $(s\times\sqrt{3})$ reconstruction. Encouragingly, the model predicts that there is a minimum in the intensity of the central peak and that the weight of the scattering moves from large to small η as the wave-vector ratio increases. However, it predicts that the minimum occurs at $\delta_K/\delta_D=0.25$ and not at 0.22. In fact, all of the measured peak intensities appear to be displaced to smaller wave-vector ratios than the model predictions. This suggests that, rather than being abrupt, the kinks are more gradual. Accordingly, we have constructed a plausible model for the structure of the chevron unit cell incorporating a gradual kink between orientational domains of the discommensuration structure. The atomic positions in the unit cell are plotted in Fig. 6(d). In the calculation, the kink is of fixed size, the discommensuration period is fixed, and the wave-vector ratio is varied by varying the separation between kinks. As a result, at the largest wave-vector ratios, the kink occupies approximately 21% of the unit-cell area, and at the smallest it is 13% of the unit-cell area. The calculated intensities based on the chevron structure model are shown as the solid lines in Figs. 12(a) and 12(b). Evidently, the model is able to quantitatively account for the observed variation of the intensity with wave-vector ratio. On this basis, it is clear that the rather dramatic intensity changes, which did not suggest *a priori* that a single structure is maintained between 300 and 865 K, may be accounted for. In addition, the chevron model accounts for the absence of peaks with observable intensity in the lower part of Fig. 6(c). In view of the simplicity of the model, we regard the overall agreement as convincing confirmation that the chevron model for the Au(111) reconstruction is correct for all temperatures between 300 and 865 K, although there remains uncertainty as to the atomic positions in the kink region.

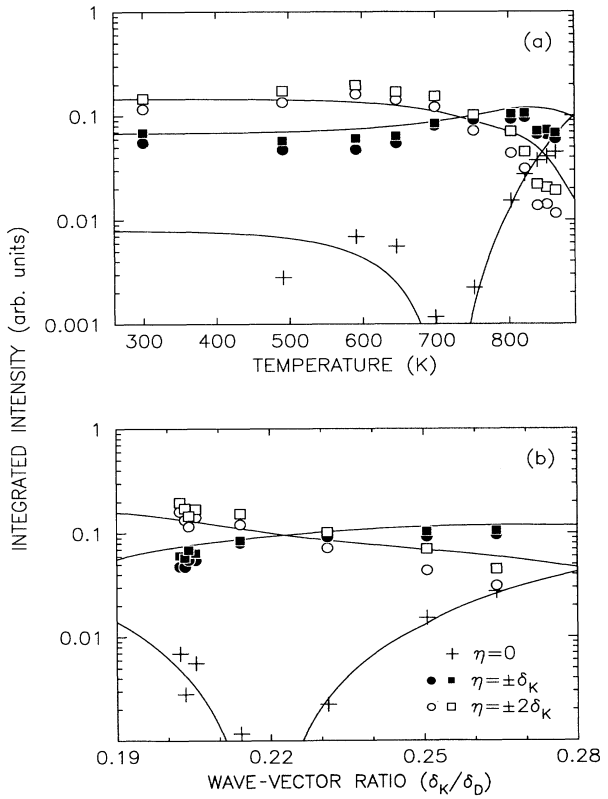

FIG. 12. Integrated intensities vs temperature for peaks transverse to $(0,1+\sqrt{3}\delta_D/2,0.12)$. Crosses are data for $\eta=0$. Solid circles are for $\eta=\delta_K$, solid squares are for $\eta=-\delta_K$, open circles are for $\eta=2\delta_K$, and open squares are for $\eta=-2\delta_K$. Solid lines were generated via a structure-factor calculation for the nonideal chevron unit cell described in the text. Integrated intensities have been plotted (a) vs temperature and (b) vs the wave-vector ratio (δ_K/δ_D).

We now briefly discuss radial scans taken through the surface rod at (0,1,0.12) and the reconstruction peak at $(0,1+\sqrt{3}\delta_D/2,0.12)$. These scans are plotted in Fig. 13. We have plotted the data obtained at 300 K as solid circles and at 850 K as open circles. For clarity, only these two temperatures are shown. From these scans (and analogous scans at intermediate temperatures) it is evi-

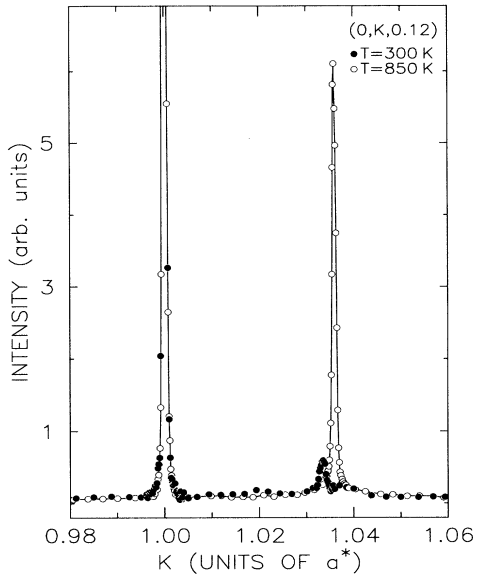

FIG. 13. Radial scans at two temperatures, 300 and 850 K. The scans pass through the surface rod at (0,1,0.12) and the reconstruction peak at $(0,1+\sqrt{3}\delta_D/2,0.12)$.

dent that δ_D increases with temperature. Also evident is the significantly greater intensity of the $\eta=0$ reconstruction peak at 850 K as compared with 300 K. For all temperatures between 300 and 865 K the radial scans are resolution limited.

The presence of an equilibrium density of kinks on the reconstructed Au(111) surface immediately suggests the existence of competing interactions, which compromise to produce a structure characterized by the new, incommensurate wave vector, δ_K. Recently, Alerhand *et al.*[15] have proposed that reconstructed, high-symmetry surfaces, which can reconstruct into one of several, rotationally equivalent structures, are unstable to the formation of domains. The origin of domain formation is the accompanying reduction of elastic stress induced in the bulk crystal. Candidates for showing this phenomenon include the (2×1) reconstructed Si(001) surface,[15,46] the reconstructed Au(111) surface,[18] and, indeed, any absorbed monolayer which forms a structure that breaks a rotational symmetry of the surface and induces an elastic deformation in the substrate. In the context of the Au(111) surface, the elastic energy is smaller for smaller kink separations, but this must be balanced against the energetic cost of locally disrupting the favorable $(s\times\sqrt{3})$ structure in the neighborhood of each kink. (It is assumed that a kink is energetically unfavorable.) The competition between these two contributions determines the kink wave vector. It is amusing to note that, since there are three possible rotationally equivalent domains of the chevron reconstruction, it, likewise, may be unstable to domain formation.

Finally, we present data that explicitly establish that only one layer participates in the chevron reconstruction. To examine the depth of a reconstruction requires that measurements be performed at large wave-vector transfers normal to the surface, i.e., large L. In the scattering geometry necessary to do this, it is not practical to make fine-resolution measurements to distinguish properly between peaks separated by only δ_K. Therefore, we have performed coarse resolution measurements (no analyzer crystal) of the overlayer reflectivity and have simply summed together the integrated intensities of individual rods. This procedure is adequate for answering the question in-hand: How many layers reconstruct? The inset to Fig. 14 shows a typical transverse scan ($L=1.80$) across the rods of scattering at $K=1+\sqrt{3}\delta_D/2$, obtained at 300 K. This profile should be compared with the profile of Fig. 7 (iii), $L=0.12$. Because of the coarser resolution employed for the scan at large L, only two peaks are apparent in the inset. Figure 14 shows the measured reflectivity obtained by integrating the intensity of both peaks at different values of L. Evidently, the reflectivity varies smoothly and monotonically with L. The scatter near $L=1$ is a result of the large thermal diffuse background emanating from the bulk Bragg reflection at $(1,0,L)$. The absence of significant modulation of the intensity as a function of L indicates that only one layer is involved in the reconstruction. Indeed, rewriting Eq. (7) for the case of a single layer characterized by lateral wave vectors different from those of the bulk, we find

$$n_s/n_i=\frac{4\pi^2r_0^2}{\Gamma^2}|F(\mathbf{Q})|^2e^{-W_0(\mathbf{Q})}|\rho_{\mathbf{Q}}(0)|^2 .$$

For the purposes of illustration, this form is shown as the solid line in Fig. 14 with $\rho_{\mathbf{Q}}(0)=1.04$; the dashed line in Fig. 14 shows the result of including a second reconstructed layer.

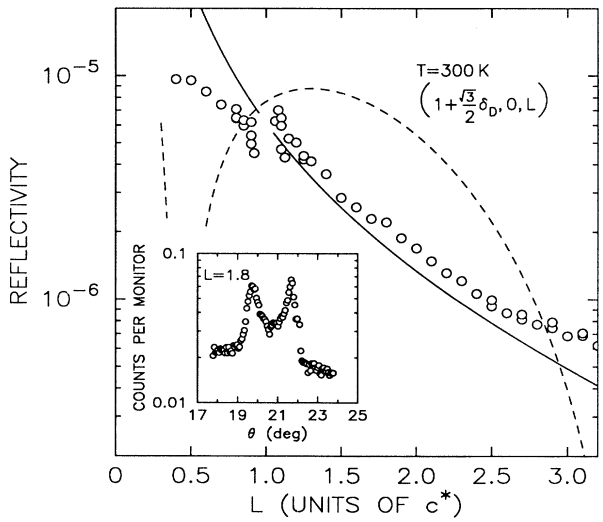

FIG. 14. Reflectivity profiles of a surface reconstruction rod. Rods summed together and plotted are those transverse to $(1+\sqrt{3}\delta_D/2,0,L)$. The gap in the data at $L=1$ is where the surface signal is overwhelmed by thermal scattering from the bulk Bragg peak at (1,0,1). Also plotted are a solid line corresponding to Eq. (7) with a single-layer reconstruction and a dashed line corresponding to a two-layer reconstruction.

C. Discommensuration fluid phase

In this section we describe measurements obtained for temperatures greater than 880 K in the discommensuration fluid phase. In this phase, the primary peaks of $S(\mathbf{Q})$ occur along each of the bulk in-plane hexagonal directions, showing that the reconstructed overlayer is now isotropically compressed. Figure 15 shows a schematic representation of reciprocal space and the high-temperature reconstruction peaks. In the figure, the solid ellipses indicate the positions of primary reconstruction peaks and the dashed ellipses are the secondary peaks, obtained from the primaries by translation through a substrate wave vector.

Figure 16 shows data typical of those obtained between 950 and 1250 K. These data were taken at glancing incidence ($L=0.12$, $\alpha=0.2°$) using the Ge(111) analyzer crystal. Figures 16(c) and 16(d) show profiles transverse to the wave-vector transfer, through the primary peak of the scattering function of the reconstructed layer; Figs. 16(a) and 16(b) show scans parallel to the wave-vector transfer. In Figs. 16(a) and 16(b), the peak at $K=1.0$ corresponds to bulk reflectivity (bulk truncation rod), while the peak at $K\cong 1.038$ corresponds to the reconstructed layer. Throughout the temperature range from 950 to 1250 K, the scattering from the reconstruction is much broader in both the radial and transverse directions than the instrumental resolution. [The radial width (HWHM) of the bulk rod at $K=1.0000$ is $\Delta Q_r=0.0002a^*$; its transverse width is $\Delta Q_\eta=0.000\,25a^*$ and is due to the sample mosaic.] Therefore, the measured scattering from the reconstruction shown in Fig. 16 represents the intrinsic scattering function [$S(\mathbf{Q})$] of the discommensuration fluid phase. Because the scattering function is broad, indicating that positional correlations are short ranged, we call this phase a discommensuration fluid. That the width of the bulk rod remains resolution limited suggests that the step-free regions of the surface still extend for greater than 5000 Å. We have fit $S(\mathbf{Q})$ in the fluid phase to a Lorentzian, allowing for different widths in the radial (κ_r) and transverse directions (κ_η):

$$S(\mathbf{Q})=\frac{B}{1+(Q_r-Q_0)^2/\kappa_r^2+Q_\eta^2/\kappa_\eta^2}\ ,$$

where Q_r and Q_η are, respectively, the in-plane radial and transverse components of $\mathbf{Q}$; Q_0 locates the peak's radial position. The best-fit profiles are shown as solid lines in Fig. 16. The parameters varied in the fits were κ_r, κ_η, Q_0, and the overall intensity (B). In addition, a constant background was included, determined by the residual scattering in the wings of the transverse profiles. For scans in both directions, a Lorentzian provides an excellent description of the experimental data.

Between 880 and 950 K the line shapes of radial scans through the reconstruction peak are unchanged from those at high temperatures and can be adequately fit with a single Lorentzian with HWHM fixed to $0.0039a^*$, as at 950 K. On the other hand, in this temperature range the transverse profiles have "shoulders" which are more pronounced for temperature increasing cycles than temperature decreasing cycles as shown in Fig. 17. We do not fully understand the origin of this line shape. However, simple calculations of the structure factor of a single chevron unit cell are suggestive of it for sufficiently small kink spacing.

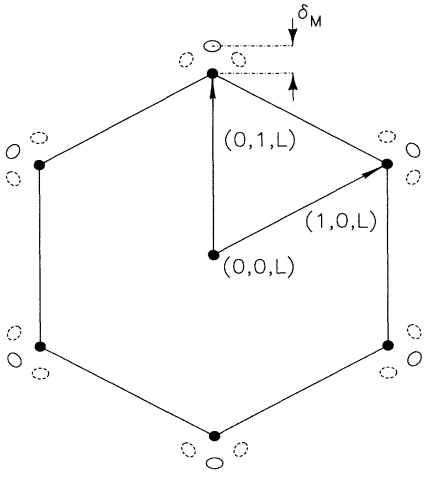

FIG. 15. Schematic representation of reciprocal space and the high-temperature reconstruction peaks. Solid ellipses are the primary reconstruction peaks. Dashed ellipses are the secondary reconstruction peaks. Secondary peaks are displaced from the primary peaks by a substrate reciprocal-lattice vector.

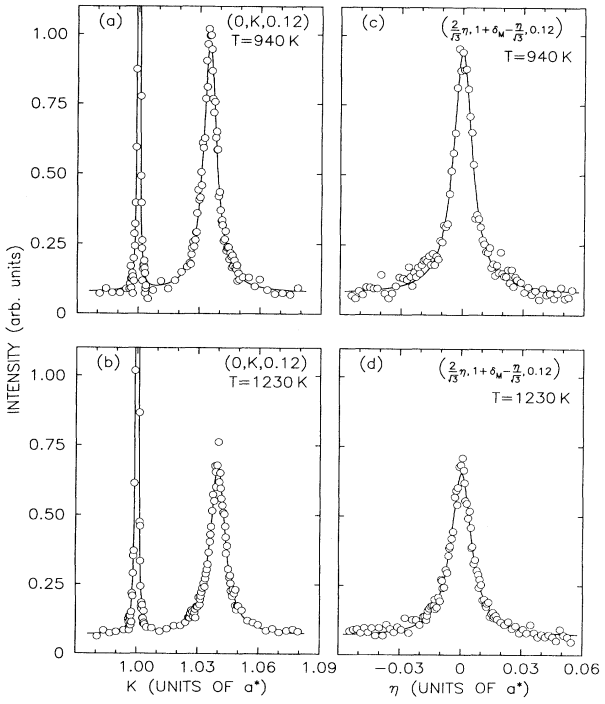

FIG. 16. Scans through the high-temperature reconstruction peak. (a) Radial and (c) transverse scans through the discommensuration fluid peak at 940 K. (b) Radial and (d) transverse scans through the discommensuration fluid peak at 1230 K. The solid lines are Lorentzian fits to the reconstruction peaks.

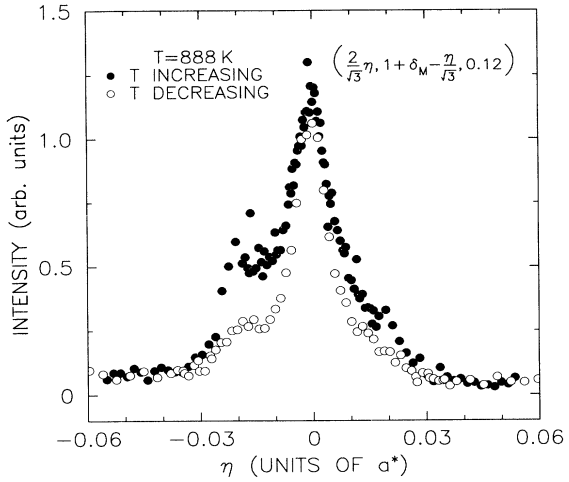

FIG. 17. Transverse scans through the reconstruction peak at $(0,1+\delta_M,0.12)$.

Figure 18(a) shows the best-fit values of the peak widths (HWHM) in the radial (solid circles) and transverse (open circles) directions, as the temperature is varied. Figure 18(b) shows the peak positions. To within the accuracy of the measurement, the peak widths (HWHM's) are constant and equal to $0.0038a^*$ in the radial direction and $0.0055a^*$ in the transverse direction. The radial peak width corresponds to a translational

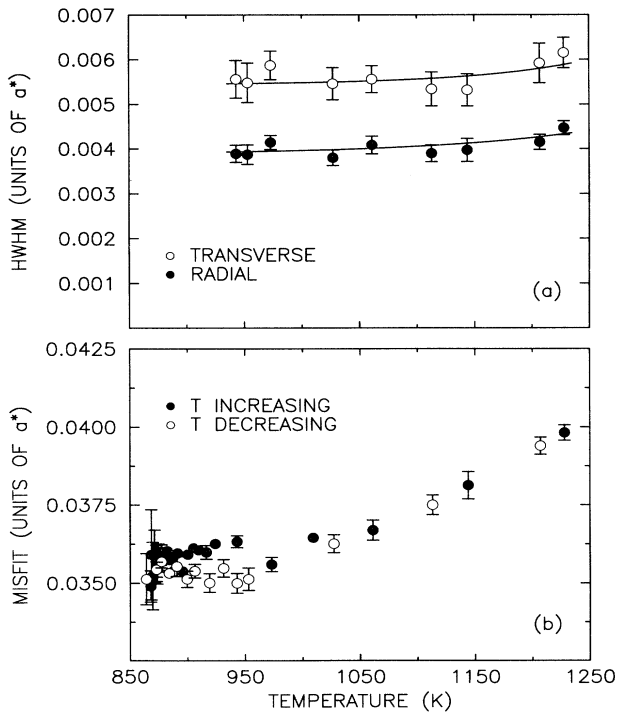

FIG. 18. Results of glancing angle measurements in the discommensuration fluid phase. (a) Half width at half maximum vs temperature for fits of Lorentzians to radial and transverse scans through the reconstruction. (b) Misfit (δ_M) of the high-temperature reconstruction peaks vs temperature.

correlation length of $\xi=36a\cong 105$ Å. We emphasize again that the extraction of this length does not involve a deconvolution procedure. It is remarkable that over a temperature range of 300 K the correlation length evolves at most only very slightly. This behavior is quite different from that observed near continuous phase transformations, where the correlation length typically decreases rapidly to a few angstroms with increasing temperature. However, an important additional length scale for the Au(111) surface at high temperatures is determined by the incommensurability (or misfit) ($\delta_M=Q_0-1$). The period of the surface unit cell is given by $L_M=4\pi/\sqrt{3}\delta_M$. As can be seen from Fig. 18(b), the misfit increases linearly (solid line) with increasing temperature; at 950 K the average surface periodicity is $L_M=28a$ and at 1250 K it is $25a$. Thus, the translational correlation length only exceeds the surface periodicity by a factor of about 1.4. In this respect, the reconstruction is very disordered. The HWHM's have not been plotted in Fig. 18(a) for temperatures between 860 and 950 K because transverse scans in this temperature range display shoulders and cannot be sensibly fit with a single Lorentzian. In addition, for consistency with our analysis of the coexistence region (Sec. III D), we chose to fit the radial profiles in this temperature range with HWHM fixed at $0.0039a^*$, which is its value at $T=950$ K. Evident in Fig. 18(b) is a suggestion of hysteresis in the temperature dependence of the misfit. This appears to be correlated with the appearance of shoulders in transverse scans through the reconstruction peak (Fig. 17).

The variation of the wave vectors with temperature in both phases implies that the overlayer contracts relative to the bulk lattice spacing with increasing temperature. To gain additional insight, we have plotted, in Fig. 19, the average area occupied by each surface atom of the Au(111) surface (solid circles), based upon the wave vectors in the discommensuration fluid phase and in the chevron phase. Specifically, we assume that the presence of kinks does not change the surface density of the chevron phase and that the density of the discommensuration fluid phase is the same as if it were a well-ordered hexagonal solid. Under these assumptions, the area per atom in the chevron phase decreases from $0.826a^2$ at 300 K to $0.824a^2$ at 865 K. Then there is a discontinuous increase in the areal density at the transformation from the chevron phase to the discommensuration fluid phase. In the discommensuration fluid phase, the area per atom continues to decrease with increasing temperature, from $0.806a^2$ at 880 K to $0.795a^2$ at 1250 K. Also shown in Fig. 19 is the area per atom for a (111) plane in the bulk (dashed line). This represents the area per atom of a commensurate, unreconstructed layer. The area per atom for the reconstructed Au(001) surface is shown as the solid line. This surface reconstructs to form an incommensurate hexagonal overlayer, in spite of the planes of square symmetry lying beneath.[40] [We have ignored the small corrugation of the Au(001) surface.[40]] Between 300 and 1170 K, at which temperature the hexagonal reconstruction disappears, the hexagonal lattice constants of the reconstructed Au(001) surface are only weakly

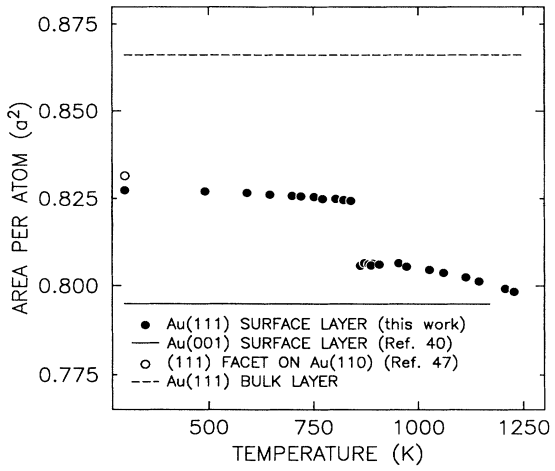

FIG. 19. Calculated area per atom for hexagonal or nearly hexagonal surfaces, exposed facets, and bulk layers of Au as a function of temperature. Solid circles are the calculated areas per atom for atoms of the Au(111) surface. There is a discontinuity in areal density at the disordering transformation.

temperature dependent relative to those of the bulk.[40] Therefore, to sufficient accuracy, the area per atom for the Au(001) surface is constant and equal to $0.793a^2$. Finally, the area per atom for gold atoms on the (111) microfacet of the (2×1) reconstructed Au(110) surface is shown at 300 K, using the structural parameters given in Ref. 47. It is striking that the area per atom of the Au(111) surface approaches that of the reconstructed Au(001) surface as the temperature increases. This suggests the possibility that a hexagonal overlayer of Au, on an Au substrate, has a natural lattice constant. Recent calculations by Dodson[12] and by Needs and coworkers[13,14] indicate that unreconstructed metal surfaces experience a tensile stress, so that the surface atoms indeed have a smaller natural nearest-neighbor separation than in the crystal interior.

Measurements of the reflectivity, presented in Sec. III A, indicate that microscopically the atomic arrangement in the discommensuration fluid phase is composed of the same unfaulted and faulted regions as in the chevron phase. A possible reconciliation of this observation with the data of the present section is that the overlayer structure is now composed of a disordered arrangement of discommensurations so that all three possible orientations of the discommensuration structure are present on length scales of order of the translational correlation length. This leads to isotropic symmetry of the overlayer. Nevertheless, the basic structural element remains the $(s\times\sqrt{3})$ motif and therefore the reflectivity profiles in the fluid phase are similar to those at lower temperatures. With this interpretation, the fluid phase may reasonably be described as a discommensuration fluid.[28–30]

In addition to the peaks of $S(\mathbf{Q})$ along the hexagonal directions (primary peaks), there are satellite peaks displaced from the primaries through a wave vector exactly equal to a substrate reciprocal-lattice vector (Fig. 15). Representative scans are shown for 970 K in Fig. 20. The small hexagons drawn as insets to Figs. 20(a) and 20(b) are analogous to that drawn about the $(0,1,L)$ rod in Fig. 6(a), except now the hexagon size is determined by δ_M. The ellipses illustrate, schematically, the secondary diffraction peak and the dashed lines indicate the scan directions through the reconstruction peak. Thus the peak shown in Fig. 20 is displaced from the primary at $(-1-\delta_M, 1+\delta_M, 0.12)$ by the (1,0,0) substrate wave vector. The widths of the peak in the scans shown in Figs. 20(a) and 20(b) are $0.0055a^*$ and $0.0038a^*$, respectively, which are identical to the transverse and radial widths, respectively, of the primary peak. This corresponds precisely to a simple translation in reciprocal space, except that the satellite peak intensity is diminished by a factor of about 2 from that of the primary (which has intensity equal to 1 on this scale). Modulated liquids have been studied in detail in the context of alkali metals intercalated into graphite.[48–50] A monolayer of Pb on a Ge substrate can also form a modulated liquid phase.[51] In these examples, the fluid correlation length is only a few angstroms and the scattering consists of a slightly modulated, diffuse *cylinder*, surrounding each substrate reciprocal-lattice vector.

It remains to discuss the origin of the excess peak

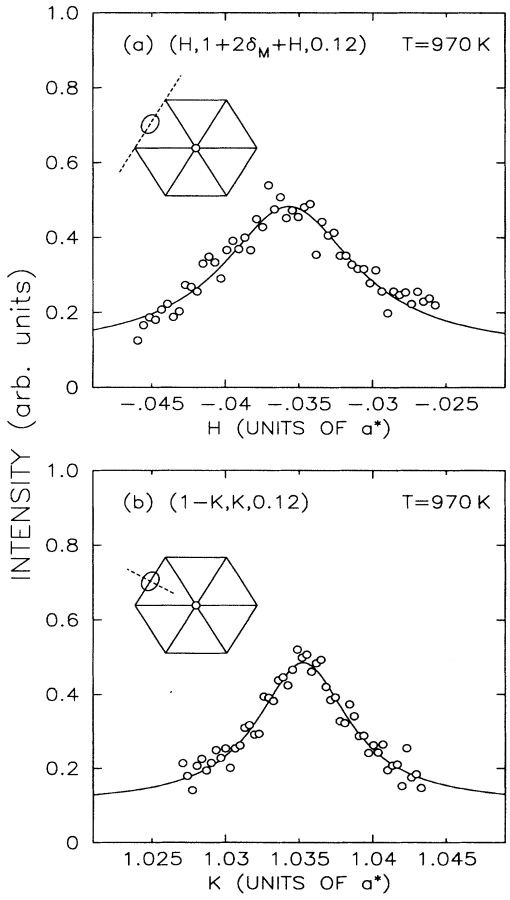

FIG. 20. (a), (b) Scans through a secondary reconstruction peak. On this intensity scale the primary reconstruction peak has intensity equal to 1.

width ($0.0017a^*$) in the transverse direction. If the peak widths were due to the decay of positional correlations alone, one would expect the radial and transverse peak widths to be the same because of the hexagonal symmetry. However, if the orientation of the discommensurations in the fluid phase fluctuates about the $\langle 1,2,0 \rangle$ directions (Fig. 3), there will be an additional contribution to the transverse width.[52,53] The magnitude of the orientational fluctuations necessary to produce the observed broadening may be estimated as $0.0017a^*/0.038a^* \cong 2.6°$ rms.

D. Phase transformation

Figure 21 shows the evolution of the radial diffraction profiles for temperatures between 866 and 879 K. At 879 K, the scattering corresponds to the discommensuration fluid phase, while at 866 K it corresponds to the chevron phase. At the intermediate temperature (872 K), there appears to be phase coexistence. At 879 K, the discommensuration-fluid-phase scattering function is broad ($\kappa_r = 0.0039a^*$) and peaked at Q_0 (fluid) $= 1.035a^*$, whereas at 866 K the width of the chevron phase peak is resolution limited ($\Delta Q_r = 0.000\,25a^*$ HWHM) and the peak position is Q_0 (chevron) $= 1.036a^*$. The different peak positions suggest that there is a discontinuous density change at the transformation from chevron to discommensuration fluid phase (see Fig. 19). This in turn requires that the phase transformation be first order. Further evidence which indicates that the transformation is first order is provided by the data obtained at 872 K (and at other intermediate temperatures). This profile appears to be composed of two distinct components—one broad and one narrow. Furthermore, the position of the narrow component is close to that of the chevron structure peak and the position of the broad component is close to that of the discommensuration-fluid-phase peak. This is exactly what one would expect for the scattering in the case of two-phase coexistence.

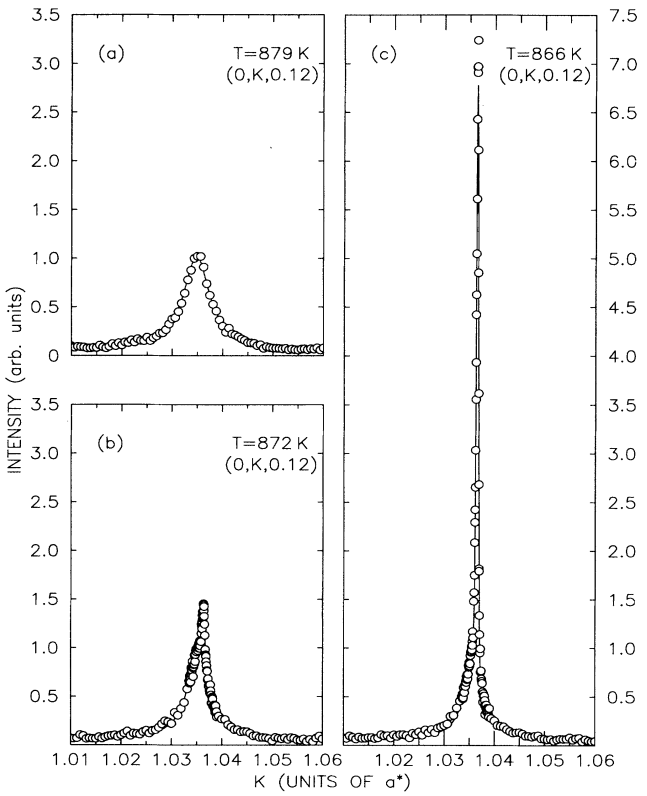

FIG. 21. Radial scans through the principal reconstruction peak in the coexistence region. (a) Scattering profile characteristic of the high-temperature discommensuration fluid phase. The solid line is a best fit to a single Lorentzian line shape. (b) Scattering profile characteristic of coexistence. A sharp peak at $K = 1.0364$ coexists with a broad fluidlike peak at $K = 1.0353$. (c) Scattering profile characteristic of the chevron phase.

To further test the hypothesis that the transformation is first order, we have fit radial scans in the region of the phase transformation to a model profile composed of the sum of a discommensuration-fluid-phase radial line shape and of a chevron phase radial line shape. The parameters allowed to vary in the fits were the two peak positions and the two peak intensities. The solid lines in Fig. 22 show the model profiles corresponding to the best-fit parameters. These fits provide an adequate description of the data and are superior to fits to a model consisting of a single Lorentzian. Figure 23 shows the results for the intensity of the chevron and discommensuration fluid scattering as a function of temperature in the neighborhood of the phase transformation. The approximately linear behavior of the intensities is as expected in a two-phase coexistence region.

It is worthwhile comparing the behavior of the Au(111) surface with that of the Au(001) surface.[40] The Au(111) reconstruction disorders at $\cong 870$ K, while the Au(001) reconstruction disorders at a significantly higher temperature (1170 K), also via a first-order transformation. At first sight, the difference between the disordering temperatures appears surprising in view of the similarity between the two reconstructed overlayers—both are nearly hexagonally close-packed structures. However, the nature of the disordered phase is quite different in the two cases. For Au(001), the x-ray data are consistent with a microscopically disordered surface[40] while for Au(111) the data are consistent with a locally ordered surface, but with a disordered arrangement of discommensurations. One reason that the Au(111) discommensuration disordering temperature may be so low is that in the disordered phase there is no longer anisotropic stress induced in the bulk crystal. Alternatively, in the case that there are only two commensurate sublattices (i.e., A sites and C sites), Refs. 28 and 29 predict that for sufficiently weakly interacting discommensurations, the stripe-domain phase is unstable to the proliferation of free dislocations at arbitrarily low temperatures and thus is always a fluid. For small repulsion between discommensurations the melting temperature is also expected to be low. It is tempting to suggest that the seemingly low disordering temperature of the Au(111) surface provides a realization of this behavior. However, the calculations of Refs. 28 and 29 are carried out for the case of widely separated discommen-

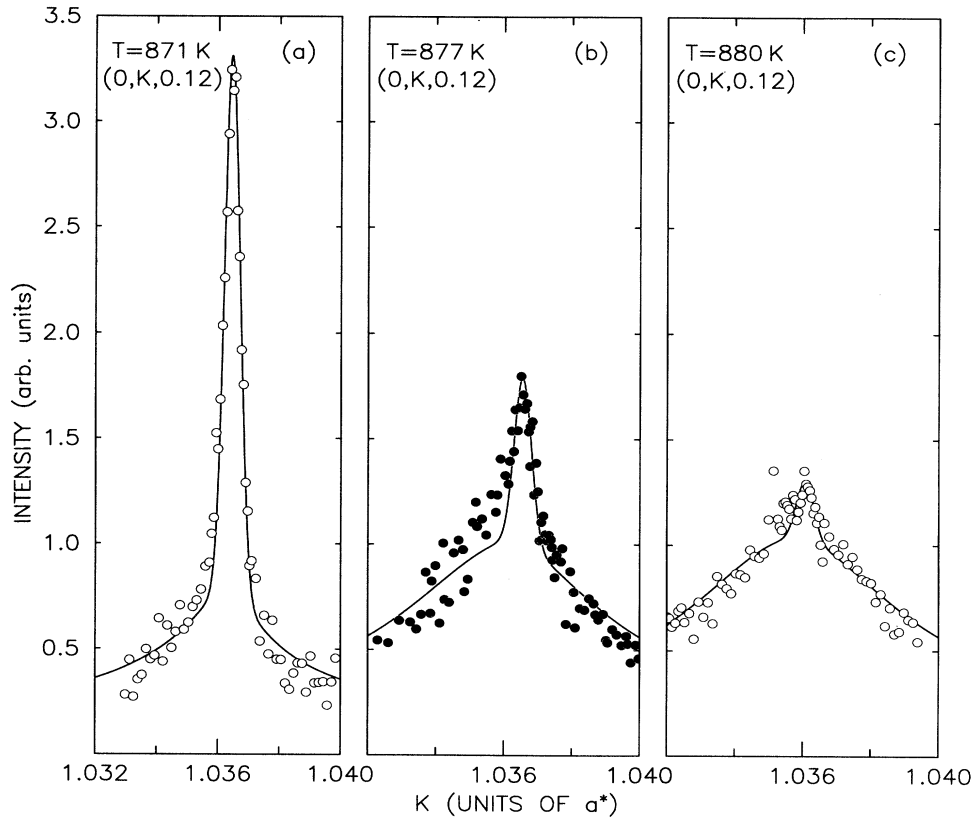

FIG. 22. Radial scans in the coexistence region. The solid lines are a best fit to a model line shape composed of the sum of a discommensuration-fluid-phase radial line shape and a chevron-phase radial line shape. Scans for (a) 871, (b) 877, and (c) 880 K.

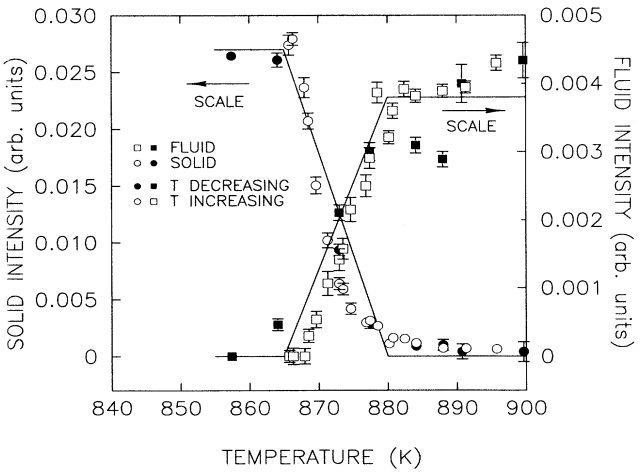

FIG. 23. The intensity of the chevron-phase peak and discommensuration-fluid-phase peaks vs temperature. Solid symbols are the measured discommensuration-fluid and chevron-phase intensities for decreasing temperature. Open symbols are the discommensuration-fluid and chevron-phase intensities for increasing temperature. The width of the coexistence region is $\Delta T \cong 15$ K.

surations and the possibility of 120° kinks is explicitly excluded. Therefore, their application to the Au(111) surface is far from straightforward. Isolated dislocations, where two discommensurations meet and end, are evident in the STM data of Ref. 17 obtained at 300 K.

IV. CONCLUSIONS

In this paper we have presented the results of a comprehensive synchrotron x-ray diffraction study of the clean Au(111) surface between 300 and 1250 K. The surface is reconstructed throughout this temperature range; however, we have found two distinct phases. For temperatures less than 865 K, the surface structure consists of an equilibrium density of kinks between rotationally equivalent domains of a uniaxial reconstruction. The uniaxial reconstruction itself is composed of a sequence of discommensurations separating surface regions with the correct fcc *ABC* stacking sequence from faulted regions with an *ABA* stacking sequence. Both the kink separation and the discommensuration separation evolve to smaller values with increasing temperature. For temperatures greater than 880 K, atomic positions are microscopically well defined. However, the arrangement of discommensurations and kinks is disordered. This gives rise to a surface structure which on the average is iso-

tropically compressed and for which the translational correlation length is comparable to the periodicity of the discommensurations. Remarkably, this structure persists to the highest temperature studied (1250 K). There is a first-order phase transformation between these two structures with a narrow (15 K) coexistence region. The x-ray reflectivity is always aligned with the crystallographic (111) planes, indicating that the (111) surface is a well-defined, smooth facet for temperatures between 300 and 1250 K.

ACKNOWLEDGMENTS

We would like to thank B. Ocko for his collaboration in the early stages of this project and G. Ownby for his invaluable assistance during the experiment. We are particularly grateful to D. Chambliss and D. Vanderbilt for useful conversations. We thank R. J. Birgeneau, S. C. Fain, Jr., M. Seul, and S. K. Sinha for helpful comments. Work performed at MIT is supported by the U.S. National Science Foundation under Grant No. DMR-8806591 (Solid State Physics Program). Research performed at Oak Ridge National Laboratory is sponsored by the Division of Materials Sciences, Office of Basic Energy Sciences, U.S. Department of Energy, under Contract No. DE-AC05-840R21400 with Martin Marietta Energy Systems, Inc. Work performed at Brookhaven National Laboratory is supported by the U.S. Department of Energy under Contract No. DE-AC0276CH00016. Beamline X20A is supported jointly by the NSF through the Materials Research Laboratory at MIT under Grant No. DMR-8719217 and by IBM. The NSLS is supported by the U.S. Department of Energy.

APPENDIX

Figure 24 shows data obtained by rocking the crystal through the reflection condition at $\mathbf{Q}=(0,0,6.18)$ (hexagonal coordinate system) for several different temperatures. Rocking curves for other values of L are qualitatively similar. At the peak in the center of the scan the reflection condition is satisfied. Evidently, this is superimposed on a strongly temperature-dependent "background" of a rather unusual shape. In fact, the background scattering is thermal diffuse scattering from bulk lattice vibrations (phonons) and the seemingly unusual form of the background is readily understood on the basis of Eq. (10) as follows. Exactly along the cubic (111) direction the factor of $(\mathbf{e}\cdot\mathbf{Q})^2$ ensures that the diffuse intensity is determined by the frequency of the longitudinal phonons. On the other hand, rocking the crystal away from this direction allows transverse phonons to contribute. Since transverse phonon frequencies are lower than those of longitudinal phonons, the diffuse intensity increases. Eventually, it decreases again because the wave vector of the contributing phonons increases, thus increasing their frequency. Indeed, the position of the maximum as a function of $\mathbf{Q}$ can be qualitatively understood on the basis of Eq. (10).

The comparison between Eq. (10) and the observed diffuse intensity is particularly simple along the specular direction. Equation (10) becomes

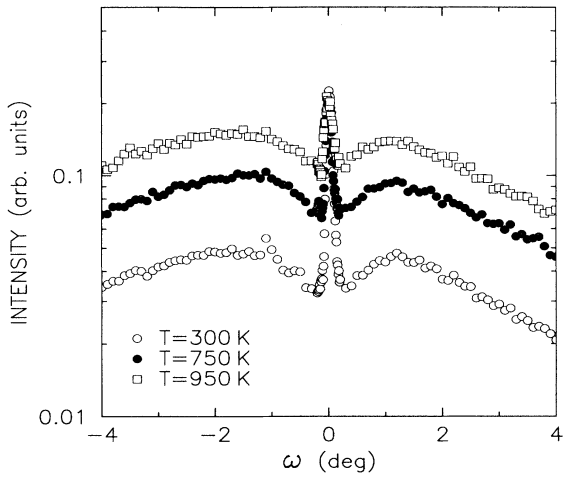

FIG. 24. Transverse scans through the specular rod at (0,0,6.18) as a function of temperature. The broad peaks at $\omega\cong\pm1.5°$ are the result of thermal diffuse scattering.

$$n_s/n_i=\tfrac{1}{2}\Lambda_0\rho_0 r_0^2|F|^2 e^{-2W}\frac{Q_z^2 k_B T}{M\omega_l^2(Q_z)}\Delta\Omega\ , \tag{A1}$$

where $Q_z=Lc^*$ is along the surface-normal direction. Fortunately, the lattice dynamics of gold have been characterized in detail by inelastic neutron scattering[54] and in particular the frequency of longitudinal phonons propagating along the cubic [1,1,1] direction (ω_l) has been measured. Thus a direct comparison between our background scattering and Eq. (A1) is possible.[55] Figure 25 shows the diffuse scattering at 750 and 1100 K along the specular direction, together with the expected

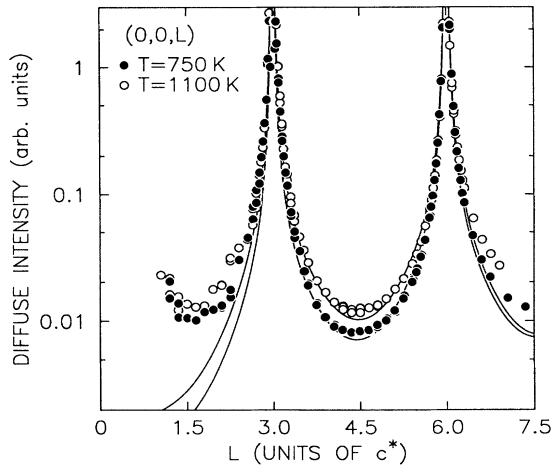

FIG. 25. Diffuse intensity along the specular rod at two different temperatures. Solid lines are fits to the thermal diffuse scattering (TDS) line shape. The deviation from theory at small L is due to air scattering.

thermal diffuse scattering calculated from Eq. (A1). The only parameter varied to obtain the evident agreement for both temperatures was an overall intensity; consideration of first-order thermal diffuse scattering alone produces reasonable agreement (Fig. 25). The discrepancy at large L may be due to second-order thermal diffuse scattering.[31,36] The discrepancy at small L is due to air scattering of the incident x-ray beam.

[1]J. Perderau, J. P. Biberian, and G. E. Rhead, J. Phys. F **4**, 798 (1974).

[2]D. M. Zehner and J. F. Wendelken, in *Proceedings of the Seventh International Vacuum Congress and the Third International Conference on Solid Surfaces,* edited by R. Dobrozemsky *et al.* (F. Berger and Söhne, Vienna, 1977), p. 517.

[3]H. Melle and E. Menzel, Z. Naturforsch. **33a**, 282 (1978).

[4]J. C. Heyraud and J. J. Métois, Surf. Sci. **100**, 519 (1980).

[5]Y. Tanishiro, H. Kanamori, K. Takayanagi, K. Yagi, and G. Honjo, Surf. Sci. **111**, 395 (1981).

[6]L. D. Marks, V. Heine, and D. J. Smith, Phys. Rev. Lett. **52**, 626 (1984).

[7]U. Harten, A. M. Lahee, J. P. Toennies, and C. Wöll, Phys. Rev. Let. **54**, 2619 (1985).

[8]W. J. Kaiser and R. C. Jaklevic, Surf. Sci. **182**, L227 (1987).

[9]C. Wöll, S. Chiang, R. J. Wilson, and P. H. Lippel, Phys. Rev. B **39**, 7988 (1989).

[10]M. M. Dovek, C. A. Lang, J. Nogami, and C. F. Quate, Phys. Rev. B **40**, 11 973 (1989).

[11]See, for example, S. G. J. Mochrie, A. R. Kortan, R. J. Birgeneau, and P. M. Horn, Z. Phys. B **62**, 79 (1985), and references therein.

[12]B. W. Dodson, Phys. Rev. Lett. **60**, 2288 (1988).

[13]R. J. Needs, Phys. Rev. Lett. **58**, 53 (1987).

[14]R. J. Needs and M. Mansfield, J. Phys. Condens. Matter **1**, 7555 (1989).

[15]O. L. Alerhand, D. Vanderbilt, R. D. Meade, and J. D. Joannopoulos, Phys. Rev. Lett. **61**, 1973 (1988). See also V. I. Marchenko, Zh. Eksp. Teor. Fiz. **81**, 1141 (1981) [Sov. Phys.—JETP **54**, 605 (1981)], and T. Garel and S. Doniach, Phys. Rev. B **26**, 325 (1982).

[16]K. G. Huang, D. Gibbs, D. M. Zehner, A. R. Sandy, and S. G. J. Mochrie. Phys. Rev. Lett. **65**, 3317 (1990); K. G. Huang *et al.*, Bull. Am. Phys. Soc. **35**, 252 (1990).

[17]D. D. Chambliss and R. J. Wilson (unpublished); J. V. Barth, H. Brune, G. Ertl, and R. J. Behm, Phys. Rev. B **42**, 9307 (1990).

[18]D. Vanderbilt (private communication).

[19]J. Villain and I. Vilfan, Surf. Sci. **199**, 165 (1988).

[20]G. A. Held, J. L. Jordan-Sweet, P. M. Horn, A. Mak, and R. J. Birgeneau, Solid State Commun. **72**, 37 (1989).

[21]I. K. Robinson, E. Vlieg, and K. Kern, Phys. Rev. Lett. **63**, 2578 (1989).

[22]J. W. M. Frenken, P. M. J. Marée, and J. F. van der Veen, Phys. Rev. B **34**, 7506 (1986).

[23]D. A. Bruce, J. Phys. C **14**, 5195 (1981); see also R. A. Cowley, J. D. Axe, and M. Iizume, Phys. Rev. Lett. **36**, 806 (1976).

[24]S. R. Andrews and R. A. Cowley, J. Phys. C **18**, 6427 (1985).

[25]I. K. Robinson, Phys. Rev. B **33**, 3830 (1986).

[26]A. M. Afanas'ev, P. A. Aleksandrov, S. S. Franchenko, V. A. Chaplanov, and S. S. Yakimov, Acta Crystallogr. A **42**, 116 (1986).

[27]For a theoretical discussion of the Au(111) surface at high temperatures, see P. Carnevali, F. Ercolessi, and E. Tosatti, Phys. Rev. B **36**, 6701 (1987).

[28]S. N. Coppersmith, D. S. Fisher, B. I. Halperin, P. A. Lee, and W. F. Brinkman, Phys. Rev. Lett. **46**, 549 (1981); Phys. Rev. B **25**, 349 (1982).

[29]J. Villain and P. Bak, J. Phys. (Paris) **42**, 657 (1981).

[30]D. E. Moncton, P. W. Stephens, R. J. Birgeneau, P. M. Horn, and G. S. Brown, Phys. Rev. Lett. **41**, 461 (1981); P. W. Stephens, P. A. Heiney, R. J. Birgeneau, P. M. Horn, D. E. Moncton, and G. S. Brown, Phys. Rev. B **29**, 3512 (1984).

[31]B. E. Warren, *X-Ray Diffraction* (Addison-Wesley, Reading, MA, 1964).

[32]A. Braslau, P. S. Perhsan, G. Swislow, B. M. Ocko, and J. Als-Nielsen, Phys. Rev. A **38**, 2457 (1988).

[33]S. G. J. Mochrie, J. Appl. Crystallogr. **20**, 1 (1988).

[34]D. Gibbs. B. M. Ocko, D. M. Zehner, and S. G. J. Mochrie, Phys. Rev. B **38**, 7303 (1988).

[35]In Ref. 25, nonspecular reflectivity was named "crystal truncation rods," and in Ref. 26 "asymptotic Bragg diffraction." We prefer to use the term reflectivity for our measurements because so doing emphasizes that specular and nonspecular reflectivity differ only by an in-plane wave-vector transfer and can be placed on the same, absolute scale.

[36]See, for example, N. W. Ashcroft and N. D. Mermin, *Solid State Physics* (Holt, Rinehart and Wilson, Philadelphia, 1976), p. 794.

[37]J. D. Jackson, *Classical Electrodynamics* (Wiley, New York, 1975), p. 281.

[38]W. R. Busing and H. A. Levy, Acta Crystallogr. **22**, 457 (1967).

[39]For a detailed discussion of the reciprocal space resolution, see R. Pynn, Y. Fujii, and G. Shirane, Acta Crystallogr., Sect. A **39**, 38 (1983); R. A. Cowley, Acta Crystallogr. A **43**, 825 (1987).

[40]S. G. J. Mochrie, D. M. Zehner, B. M. Ocko, and D. Gibbs, Phys. Rev. Lett. **64**, 2925 (1990); D. Gibbs, B. M. Ocko, D. M. Zehner, and S. G. J. Mochrie, Phys. Rev. B **42**, 7330 (1990); B. M. Ocko, D. Gibbs, K. G. Huang, D. M. Zehner, and S. G. J. Mochrie, Phys. Rev. B (to be published).

[41]Huber goniometers are manufactured by Huber Diffraktionstechnik G.m.B.H., Rimsting, Federal Republic of Germany.

[42]B. M. Ocko and S. G. J. Mochrie, Phys. Rev. B **38**, 7378 (1988).

[43]J. C. Heyraud and J. J. Metois, Acta Metall. **28**, 1789 (1980).

[44]I. K. Robinson, W. K. Waskiewicz, R. T. Tung, and J. Bohr, Phys. Rev. Lett. **57**, 2714 (1986).

[45]J. D. Axe, in *Ordering in Strongly Fluctuating Condensed Matter Systems,* edited by T. Riste (Plenum, New York, 1980).

[46]F. K. Men, W. E. Packard, and M. B. Webb, Phys. Rev. Lett. **61**, 2469 (1988).

[47]M. Copel and T. Gustafsson, Phys. Rev. Lett. **57**, 723 (1986).

[48]R. Clarke, N. Caswell, S. A. Solin, and P. M. Horn, Phys.

Rev. Lett. **43**, 2018 (1979).
[49]G. Reiter and S. C. Moss, Phys. Rev. B **33**, 7209 (1986).
[50]S. C. Moss, G. Reiter, J. L. Robertson, C. Thompson, J. D. Fan, and K. Ohshima, Phys. Rev. Lett. **57**, 3191 (1986).
[51]F. Grey, R. Feidenhans'l, J. Skov Pederson, M. Nielsen, and R. L. Johnson (unpublished).
[52]G. Aeppli and R. Bruinsma, Phys. Rev. Lett. **53**, 2133 (1984).
[53]S. E. Nagler, P. M. Horn, T. F. Rosenbaum, R. J. Birgeneau, M. Sutton, S. G. J. Mochrie, D. E. Moncton, and R. Clarke, Phys. Rev. B **32**, 7373 (1985).
[54]J. W. Lynn, H. G. Smith, and R. M. Nicklow, Phys. Rev. B **8**, 3493 (1973).
[55]We expect the contribution from Compton scattering to be negligible for gold, because the Compton scattering cross section scales with Z ($Z=79$), rather than Z^2 [Eq. (9)].